Report on Czech COSPAR-related activities in 2024-2025

This report summarizes selected results of Czech institutions represented in the Czech National Committee of COSPAR and of some other bodies, namely the Institute of Atmospheric Physics (IAP) of the Czech Academy of Sciences (CAS), the Astronomical Institute (ASU) of CAS, the Faculty of Mathematics and Physics of the Charles University (FMP CU), the Masaryk University, and the Czech space industry companies joined in the Czech Space Alliance. Both selected scientific results and Czech participation in space experiments are reported.

Participation in space experiments

Astronomical Institute of the Czech Academy of Sciences (ASU CAS):

Solar Orbiter. Solar Orbiter is a flagship solar physics mission of ESA, launched in February 2020 to investigate the Sun and the inner heliosphere from unprecedented proximity. The spacecraft approaches the Sun to about 0.28 astronomical units, closer than Mercury's orbit, enabling high-resolution observations while enduring extreme thermal and radiation conditions. Through repeated gravity assists at Venus and Earth, Solar Orbiter gradually increases its orbital inclination, ultimately exceeding 30 degrees relative to the ecliptic. This allows the first direct observations of the Sun's polar regions, essential for understanding the solar magnetic cycle and dynamo processes. The payload consists of ten instruments, combining remote-sensing telescopes observing the solar atmosphere with in-situ instruments measuring particles, magnetic fields, and plasma waves. ASU CAS was involved in building three scientific instruments for the Solar Orbiter ESA mission: hard X-ray telescope STIX, coronagraph METIS and plasma wave detector RPW. Current involvement is in scientific analyses of observations.

NewATHENA. In 2019, the Czech team became a member of the international instrumentation consortium of the X-ray Integral Field Unit (X-IFU), the main instrument planned for the ESA large X-ray mission ATHENA (Advanced Telescope for High Energy Astronomy), recently re-designed as NewATHENA mission. The X-IFU instrument will use a novel technique of X-ray calorimetry to precisely measure energies of X-ray photons. The international consortium is led by France. It has 13 countries participating in the consortium. The Czech team is responsible for delivering Row Addressing Synchronization module. ASU CAS is responsible for the project management and also for scientific simulations for the instrument. IAP CAS is responsible for the development of the electronics. In 2021, ASU CAS got involved in development of the other detector onboard ATHENA mission, Wide Field Imager (WFI). The Czech team is responsible for the development of the Galvanic Isolation Modules (GIM). Two fully functional units of GIM Demonstrator Model were delivered to WFI consortium in 2025 for later AIT activities leading to Mission Adoption Review scheduled by ESA to mid of 2027.

Fig. 1. ESA NewATHENA DE GIM BBM.

LISA. Czechia is responsible for the development of the Fiber Switch Unit Actuators (FSUA), critical elements for the LISA Optical Bench. The FSUA uses piezo mechanisms to precisely

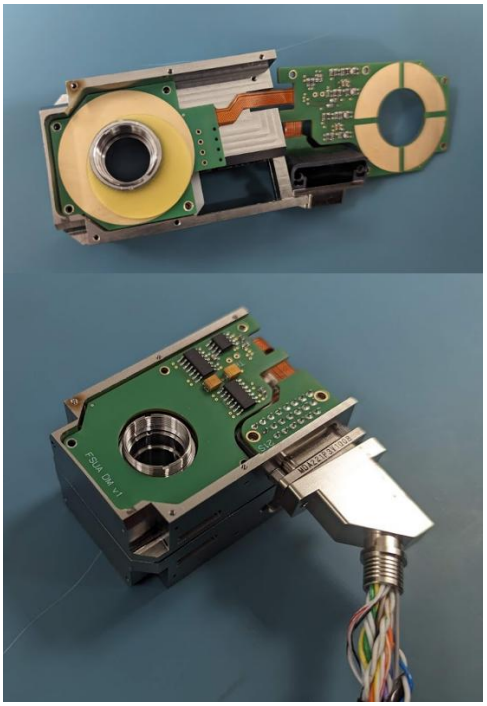

Fig. 2. FSUA demonstration model.

rotate an optical element mounted in these mechanisms. By this rotation, the FSUA will be effectively able to switch between two sources of the laser beam, which guarantees the redundancy of the laser source. Apart from the mechanism itself, also the driving electronics and the box for the Mission Control Unit will be delivered. The Czech FSUA consortium involves four institutes of CAS: ASU, Institute of Physics, IAP, and Institute of Thermomechanics. The developed mechanism passed the Preliminary Design Review in 2025. The Czech team that includes the FSUA engineering team as well as the gravitational wave

researcher is a recognized stand-alone unit in the LISA consortium that was re-structured in 2025.

IXPE. The Czech scientific team is also involved in the exploratory NASA/Italian mission IXPE (Imaging X-ray Polarimetry Explorer) that was launched in 2021. The Czech team is participating in the data X-ray polarimetry analysis and proposing new observations. Since 2024 the mission has operated the guest-observer program with observations being selected based on the peer-review. The first selected observation was observation of a newly discovered X-ray black-hole binary, Swift J1727.8-1613, led by ASU team. The new observations led to two publications in the Astrophysical Journal Letters (Svoboda J., Dovčiak M., Steiner J. et al., 2024, ApJ, 966L, 35S; Podgorný J., Svoboda J., Dovčiak M. et al., 2024, ApJ, 686L, 12P).

PLATO. PLATO is a medium-class ESA mission dedicated to search for exoplanets with method of transit detection in photometric light curves. PLATO is scheduled for launch in January 2027. The main scientific objective of PLATO is finding of terrestrial planets in habitable zones around Sun-like stars. However, PLATO will be able to answer also many further topics of exoplanetary but also stellar science. The Czech participation is led by ASU CAS with the main industrial partner SAB Aerospace. The hardware contribution were transport containers for PLATO cameras and the parts of the software for various aspects of the mission. Furthermore, the Czech companies MORAVIAN INSTRUMENTS and SAB Aerospace as subcontractors, delivered service module for PLATO and CCDs used for optical testing. As a contribution to PLATO ground based follow-up segment, ASU is leading the PLATOSpec spectrograph project installed at La Silla, Chile. PLATOSpec will be heavily involved in the PLATO candidate validation process.

PROBA-3. Proba-3 is a pioneering mission of the European Space Agency, launched in December 2024 to demonstrate high-precision formation flying in space. The mission comprises two satellites maintaining a separation of 144 meters with millimeter-level accuracy, together forming a distributed solar coronagraph named ASPIICS. One spacecraft carries an external occulter acting as an artificial Moon, while the second hosts the coronagraph telescope. This configuration enables routine observations of the solar corona down to approximately 1.1 solar radii, a region previously observable only during rare total solar eclipses. The inner corona is crucial for studying the early development of coronal mass ejections and the origin of the solar wind, both central to space-weather research. Following in-orbit commissioning and formation-flying validation, the ASPIICS coronagraph achieved its first scientific observations in mid-2025 and will continue to observe solar corona in unprecedented detail at least until the end of 2026. In addition to its scientific goals, Proba-3 represents a key technological milestone for future distributed space observatories. The Czech Republic, including ASU CAS, has made a substantial contribution to the ASPIICS coronagraph, including major roles in its design, development, and scientific exploitation.

Swarm. ESA mission of three satellites launched into low Earth orbit in 2013 to observe Earth's magnetic field. Thanks to the excellent spacecraft health, operations are planned to continue through the current solar cycle, potentially until 2031. In addition to magnetometer data, Swarm provides high-precision GPS observations that enable recovery of monthly gravity field variations at a spatial resolution of about 1500 km. Available since 2014, these gravity models are independent of dedicated gravimetry missions and effectively bridge the data gap between GRACE and GRACE-FO, as well as shorter interruptions in their records. Given the continued performance of the satellites, Swarm may also help mitigate future data gaps in GRACE-FO and upcoming gravimetric missions (GRACE C/MAGIC). The Astrodynamics

and Space Geodesy group at ASU CAS is part of a five-institution consortium producing the official Swarm gravity field products, which are released quarterly via ESA and ICGEM.

Institute of Atmospheric Physics of the Czech Academy of Sciences (IAP CAS):

We have continued our involvement in the planning of new spacecraft missions and development of new scientific spacecraft instrumentation. We have also worked on calibration and operations of spacecraft instruments and subsystems built by our team in the past.

Solar Orbiter. The European Space Agency (ESA) Solar Orbiter mission to the inner heliosphere carries a Radio and Plasma Waves instrument (RPW), which includes a Time Domain Sampler (TDS) subsystem developed at the IAP CAS in Prague. The instrument, including the TDS module, has been operating successfully since the beginning of the mission. We continued to run operations of the RPW instrument on Solar Orbiter.

Comet Interceptor. The scientific and engineering team at IAP CAS continued preparing an important hardware contribution to the future Comet Interceptor mission of ESA, which aims to investigate a dynamically new comet during its first approach to the Sun. IAP CAS is developing a Dust and Data Processing Unit.

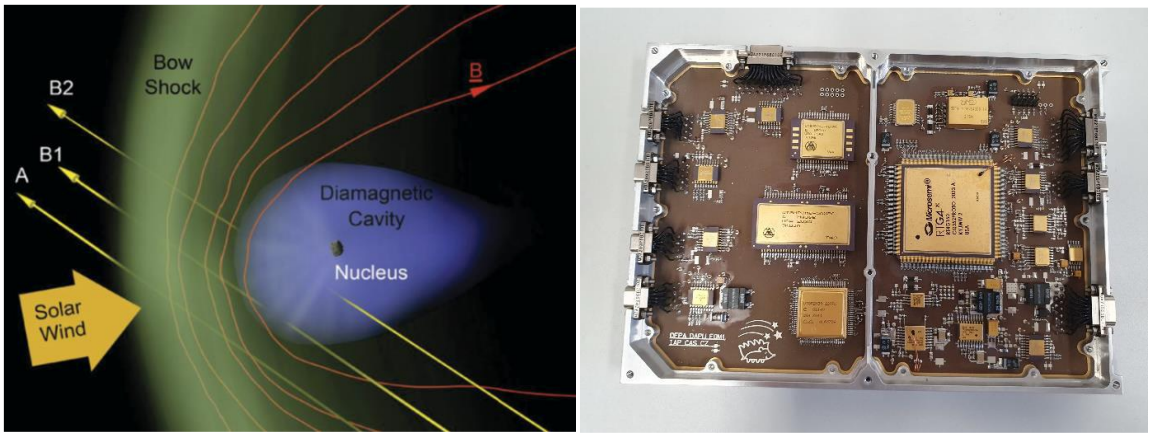

Fig. 3. a) Multi-point measurements will determine the scale and shape of several structures in the comet-solar wind interaction. The time at which each of the three spacecraft/probes cross (or do not cross) the bow shock (green) and diamagnetic cavity (blue) will determine their shapes and scales. The magnetic field (red) will also be probed using magnetometers on all the three platforms. b) Electronic board of the engineering model of the DAPU (Dust Analyzer & Processing Unit) instrument developed at IAP CAS for the probe A.

JUICE. IAP CAS is Co-PI team in the RPWI (Radio and Plasma Waves Investigation) instrument of the ESA JUICE mission. The mission was launched in 2023, aiming at investigation of the Jovian system and its three Galilean icy moons (Europa, Ganymed and Callisto). We continue our activities in in-flight calibration, software development and mission planning for the RPWI instrument on the spacecraft.

New Athena and LISA. IAP CAS is also involved in development of space electronics for the large astrophysics missions of ESA, New Athena and LISA, in collaboration with other institutes of the Czech Academy of Sciences

Cluster. Reception of the telemetry data of the WBD instrument onboard four ESA Cluster spacecraft continued in the Panska Ves station of the IAP CAS till the end of the mission after the reentry of the first Cluster spacecraft in September 2024. The data were processed at IAP CAS and submitted to international scientific community.

Plasma Observatory and M-Matisse. We have contributed to two proposals of the new ESA M-class missions, Plasma Observatory (spacecraft constellation to investigate plasma in the magnetosphere and solar wind), and M-Matisse (mission to explore space plasma around Mars).

Faculty of Mathematics and Physics of the Charles University (FMP CU)

Solar Orbiter. In February 2020, the ESA mission Solar Orbiter started its several year journey to the Sun. After two Venus flybys in 2022 and 2025 the probe is able to observe the Sun from vantage points over 15 degrees above the ecliptic. Charles University had been involved in development of the SWA/PAS proton and alpha particle sensor that initially delivered 3D ion velocity spectra with 4 s time resolution (normal mode). The SWA flight software improvement in 2024 and 2025 has allowed 2 s and 1 s resolution to be used regularly. Moreover, since the end of 2025 SWA/PAS provides 500 ms resolved 3D spectra during burst mode 8 times per day.

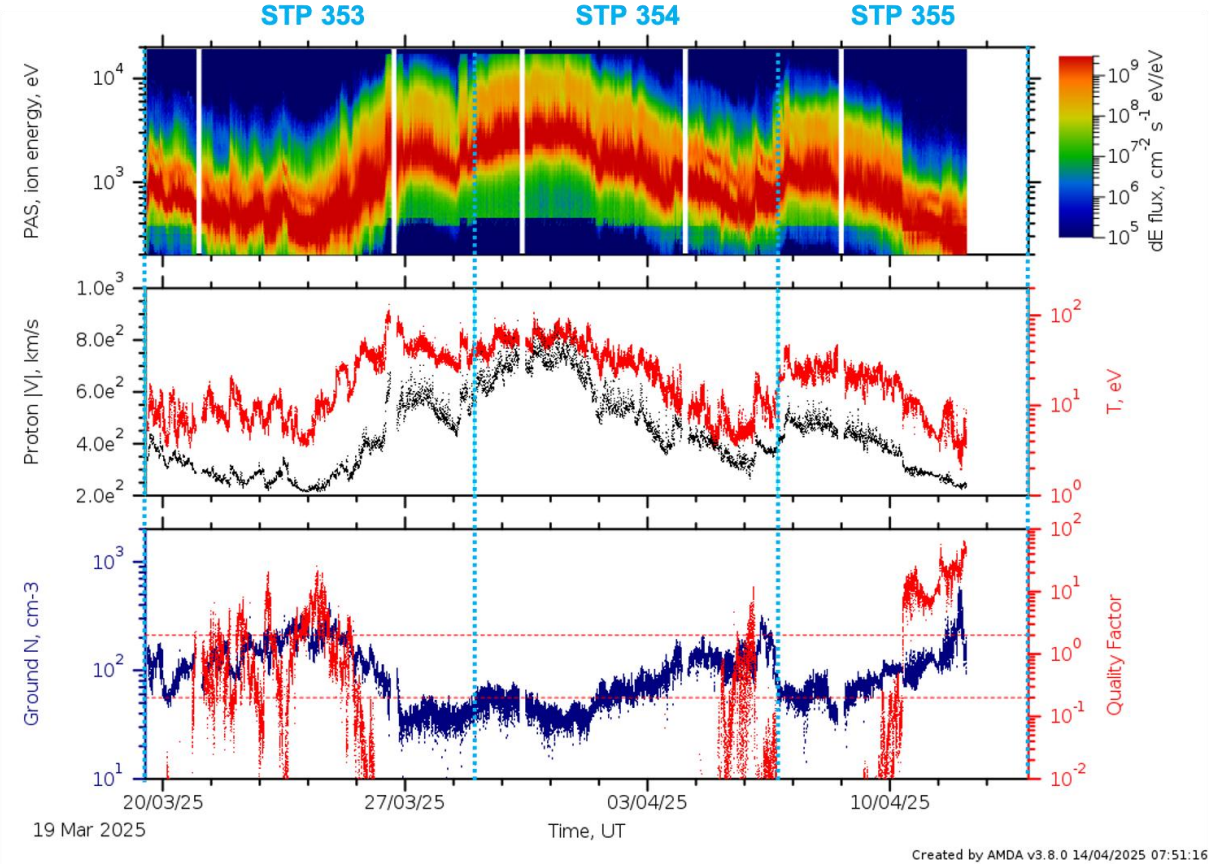

Fig. 4. Solar Orbiter SWA/PAS perihelion observation of the slow and fast wind interaction regions with 1s time resolution in March-April 2025.

Comet Interceptor. FMP CU has been involved in the ESA Fast mission Comet Interceptor aiming to flyby near a dynamically new object (a comet or an extra-solar origin body) since

2019. In this mission we have provided part of the electronics of the low energy electron spectrometer LEES led by IRAP Toulouse. During the 2024-2025 years this mission continued in Phases C/D, the launch is currently planned in 2029.

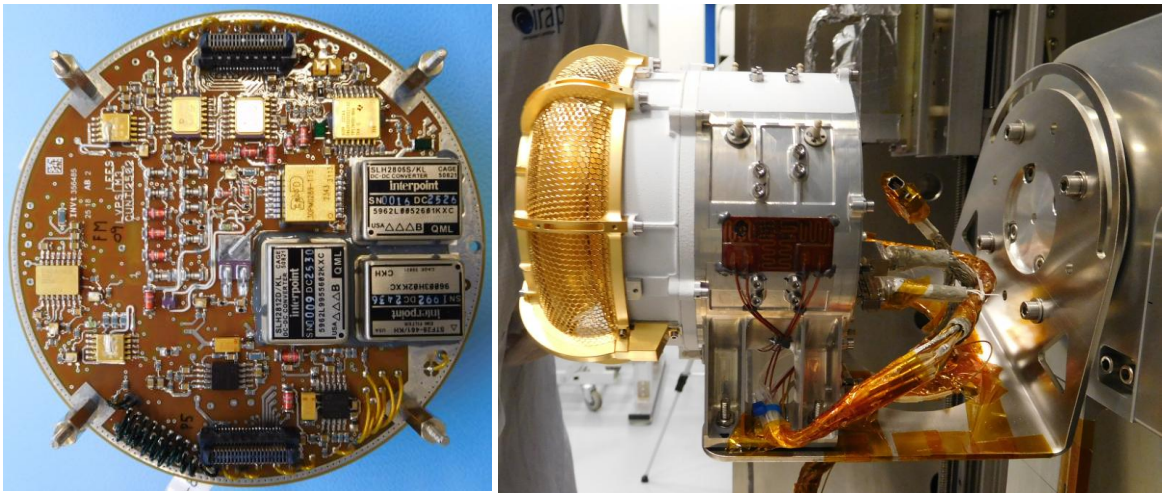

Fig. 5. The LEES low-voltage power supply flight board developed at Charles University and the LEES EQM model during functional tests in IRAP Toulouse.

HENON. During 2024-2025 Charles University also worked on development of the Faraday-cup based solar wind monitor for the HENON cubesat (ASI/ESA). It will orbit along a Distant Retrograde Orbit (DRO) of the Sun-Earth system, thus it will stay for a long period of time very far upstream of the Earth (well beyond L1 at ~ 0.1 AU from the Earth). After its expected launch in 2027 with the ESA Plato spacecraft, the HENON cubesat is expected to make a significant leap forward in the Space Weather (SWE) forecasting and science.

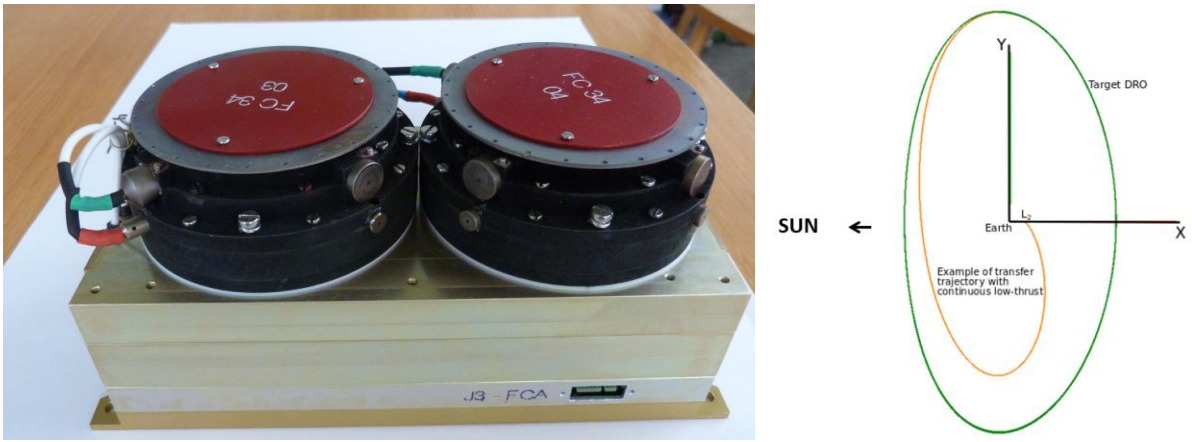

Fig. 6. The FCA EQM/FS model of the solar wind monitor instrument for the HENON mission before the functional test at Charles University (left) and the HENON assumed orbit (right).

Masaryk University

GBR detectors. Masaryk University was involved in the development of GRB detectors and led the data analysis from the GRBAlpha, GRBBeta, and VZLUSAT-2 CubeSat missions. The missions carried on board detectors that detected gamma-rays in the range of 30-900 keV,

consisting of a 56 cm2 5 mm-thick CsI(Tl) scintillator read out on one side by a set of 8 Hamamatsu multi-pixel photon counters (Pal et al. 2023, A&A, 677, 40). The missions allowed the characterization of SiPM degradation due to particles encountered in polar orbit (Ripa et al. 2025, NIM-A, 1076, 170513), and the satellites demonstrated that gamma-ray bursts can be routinely detected by CubeSat class missions. Over its lifetime, GRBAlpha detected 227 transient events, VZLUSAT-2 146 transients, and the GRBBeta satellite, launched in 2024, has so far detected around 20 events (Ripa et al. 2026, arXiv: 2601.16609).

QUVIK. The Czech Republic leads the development of a 2-band UV space telescope mission called QUVIK. The small, 200 kg class mission will carry two ~25 cm telescopes for the near- and far-UV bands and a gamma-ray burst detector. The mission's science lead is at Masaryk University, and the industrial consortium is led by VZLU Aerospace. International partners include an Italian consortium led by ASI and INAF developing the FUV payload, the Dunlap Institute at the University of Toronto, and Technion in Israel. The satellite, expected to launch in 2031, will observe energetic stellar explosions, stars, as well as active galactic nuclei.

Czech Space Alliance (CSA)

The CSA is an industry association of and for Czech companies with proven capabilities and track records in the space business and a broad international customer base. The main objectives are to represent and promote the interests of the space industry to national decision-makers and participate in the co-creation of national space policy. The association presents the capabilities of its members at international events and helps them to develop business relationships with potential international partners in Europe and beyond. https://www.czechspacealliance.eu/

5M	flexible solar arrays for large telecom satellites, solar panel for ESA mission to Saturn's moon Enceladus, technologies for the landing legs of future European launch vehicles and structural panels for the ESA ROSE-L satellite
Advacam	cameras based on CERN Timepix chip for radiation imaging, spectrometry, dosimetry and particle tracking; six radiation detectors for NASA Artemis II Moon mission; radiation early warning system for satellite constellations
BBT	special optics and cameras based on calomel crystals, high efficiency infrared polarizers, acoustooptical tuneable filters (AOTF) for hyperspectral imaging in the thermal infrared based for industrial and dual-use applications
BD Sensors	APplication Module Electronic (APME) unit for ESA JUICE mission to Jupiter, Banks Of SuperCapacitors (BOSC) for power demands of telecom satellites, pressure sensors for ESA I-HAB module for Lunar Gateway
CGI	Earth observation services and support to infrastructure operators and companies, web application integrating Copernicus data and services

	with analytical methods for environmental monitoring and risk assessment
EGGO Space	evaluation testing of passive EEE components (capacitors, resistors, relays) according to ESCC standards, climatic, mechanical and life time testing in thermal chambers, vibration and mechanical shock apparatuses
ESC Aerospace	Multipurpose Drive Electronics to control movement of solar panels, antennas or scientific instruments; EGSE/SCOE test systems, QKD trusted node, space qualified SW, on-board computers, radiation monitors, hyperspectral camera
Frentech Aerospace	solar panels' and antenna pointing deployment mechanisms, cargo door mechanisms, fine rotary actuators, reaction wheels, valves, pumps, mirror support structures, cryostat structure, magnetic divertor, landing gears
HULD	AI powered on-board software and data processing, mission control system (MCS), software defined GNSS receiver TIRA, distributed and quantum computing, satellite constellation information sharing system
Iguassu SS	core expertise in GNSS/SBAS, GNSS performance monitoring, robotic & fly-eye telescope test bed for asteroid detection, Ariane 6 telemetry onboard processing and ground segment software, satcom software
L.K. Engineering	structural and thermal analysis to design spaceflight hardware, computation of launcher aerodynamics, aeroelasticity and acoustics, R&D projects or the design of ground support equipment including additive manufacturing
OHB Czechspace	mechanical design of structural items and systems, structural analysis and verification of structural items, sub-assemblies, satellite systems, electronic equipment, ESA SOVA Scout mission for observing Earth's atmosphere
Rigaku Innov. Technologies Europe	X-ray optics - Lobster Eye, Kirkpatrick-Baez system, ellipsoidal, parabolic and Wolter I optics, cameras and telescopes equipped with X-ray detectors, optical payload at VZLUSat-1 and VZLUSat-2 satellites
SAB Aerospace	structural subsystem design and integration, small satellite dispensor for Vega and sequencer for Ariane 6 launcher, IOSHEX in-orbit servicing system, satellite structure for the ESA Plato SVM and ROSE-L satellite
Stratosyst	engineering solutions for applications in the stratosphere & harsh environments, high-altitude platform stations (HAPS) and its payloads (Earth observation, telecommunications, local GNSS augmentation, defense)
Streicher Plzeň	engineering and manufacturing of thermal-vacuum chambers of all sizes, modular TVC systems, small hexagonal chamber for ESA ESTEC

	operating from -180°C to 200°C, vacuum coating, assembly in ISO 6 and ISO 8 clean rooms
TERMA	mission control system (MCS) & ground station software; central checkout systems (CCS), electrical ground support equipment (EGSE); power, thermal, & instrument SCOE, functional and performance testing of a spacecraft
Toseda	custom design, development and commercialization of high tech polymeric and nanocomposite materials (composites, adhesives, elastomers, coatings, foams, aerogels, sensors) with special customer defined properties
TTS	custom-made thin films for electronic and optical applications, thin film metallization and production of components by magnetron sputtering, ion beam etching and UV photolithography, simulations of space radiation effects
Unites	Automated testers for semiconductor devices and FCT/ICT platform for assembled PCB testing, laboratory systems for testing of transistors, diodes, ICs, memories, relays, VLSI, testing discrete semiconductors in production

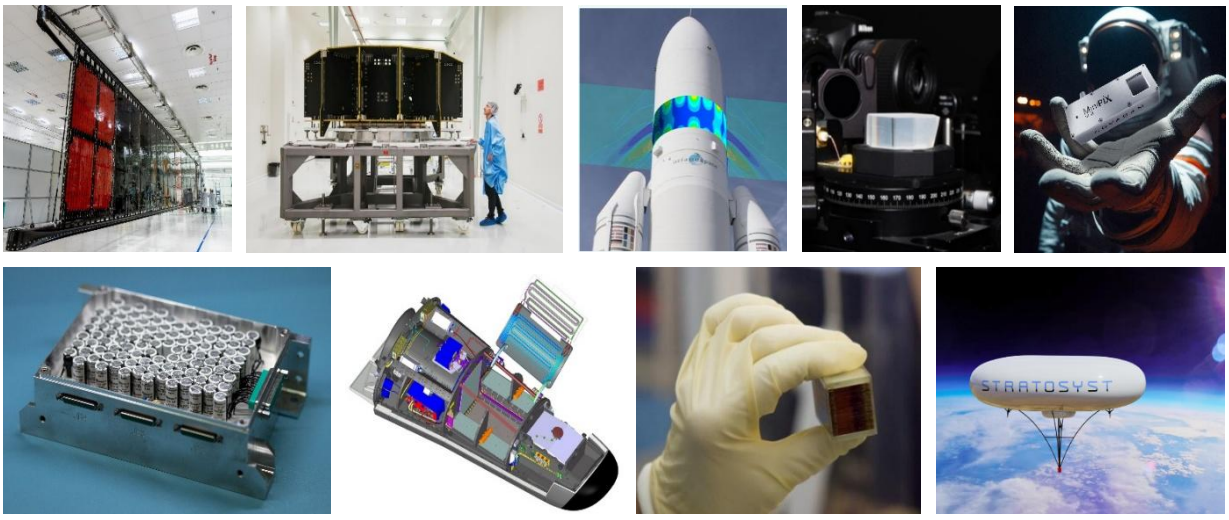

Selected scientific results

Institute of Atmospheric Physics of the Czech Academy of Sciences (IAP CAS):

Strong effects of chorus waves on radiation belts expected for future magnetic superstorms

We employed extensive databases of spacecraft observations to determine how lower-band whistler mode chorus waves behave under extreme geomagnetic conditions. Chorus occurring close to the geomagnetic equator is known for causing rapid increases of ultra-relativistic electron fluxes under disturbed geomagnetic conditions. However, chorus can also propagate to high latitudes and here its presence may lead to losses of these electrons. We showed that under extreme geomagnetic conditions, amplitudes of chorus waves at high latitudes grow much slower than chorus amplitudes close to the equator. They therefore have a net effect of accelerating ultra-relativistic electrons, which results in an increase of fluxes at multi-MeV energies by several orders of magnitude.

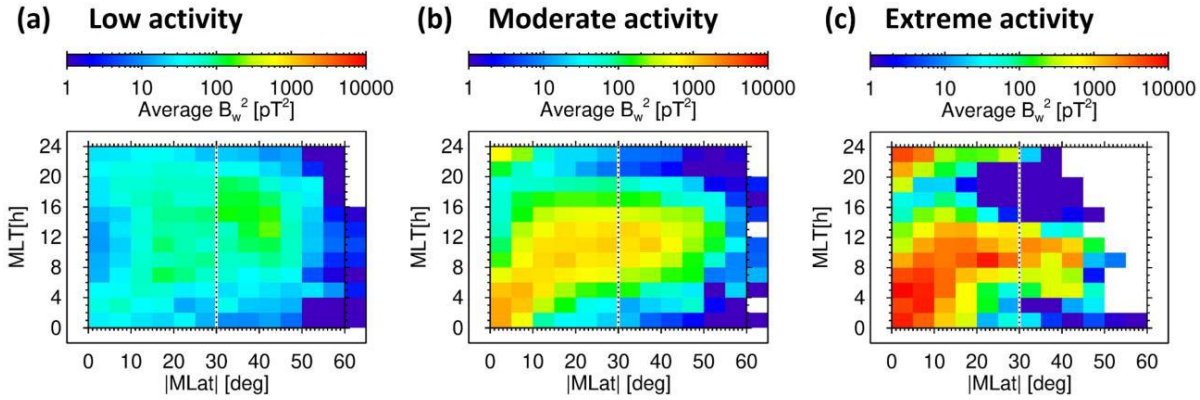

Fig. 7. External driving of chorus. Color scale shows the long-term average squared amplitudes of chorus magnetic field fluctuations in pT2. A joint data set of two Van Allen Probes and four Cluster spacecraft is analyzed in 12x13 discrete bins in magnetic local time and absolute value of magnetic latitude, where cumulative results for latitudes above 60° are shown on the outer edge of the plot. (A) Data from periods of low geomagnetic activity: see Supplementary Method 4; (B) the same for moderate geomagnetic activity; (C) the same for extreme cases of the highest geomagnetic activity. A vertical dotted line shows an approximate boundary between the equatorial region, where chorus strongly responds to geomagnetic activity, and the high-latitude region, where the response is weak.

Santolík, O., Shprits, Y., **Kolmašová, I.**, Wang, D., **Taubenschuss, U.**, **Turčičová, M.**, & **Hanzelka, M.** (2024). Strong effects of chorus waves on radiation belts expected for future magnetic superstorms. *AGU Advances, 5*, e2024AV001234. https://doi.org/10.1029/2024AV001234

Němec, F., **Santolík, O**., Hospodarsky, G. B., & Kurth, W. S. (2024). Magnetospheric line radiation: Temporal modulation corresponding to a bouncing wave. *Geophysical Research Letters, 51*, e2024GL111477. https://doi.org/10/1029/2024GL111427

Němec, F., **Santolík, O.**, Hospodarsky, G. B., & Kurth, W. S. (2024). Quasiperiodic emissions: Fine structure corresponding to a bouncing wave. *Geophysical Research Letters, 51*, e2023GL106459. https://doi.org/10.1029/2023GL106459

Whistler echo trains triggered by energetic winter lightning

Lightning generated electromagnetic impulses propagating in the magnetospheric plasma disperse into whistlers – several seconds long radio wave signals with decreasing frequency. Sometimes, multiple reflections form long echo trains containing many whistlers with increasing dispersion. On January 3, 2017, two necessary prerequisites – a pronounced lightning activity and a magnetospheric plasma duct – allowed for observations of a large

number of whistler echo trains by the high-latitude station in Kannuslehto, Finland. Our investigation reveals that the duct existed for nearly eight hours. We show that causative lightning sferics arrived to the duct entry from three different winter thunderstorms: a small storm at the Norwegian coast, which produced energetic lightning capable to trigger echo trains in 50% of cases, and two large storms at unexpectedly distant locations in the Mediterranean region. Our results show that intense thunderstorms can repetitively feed electromagnetic energy into a magnetospheric duct and form whistler echo trains after subionospheric propagation over distances as large as 4000 km.

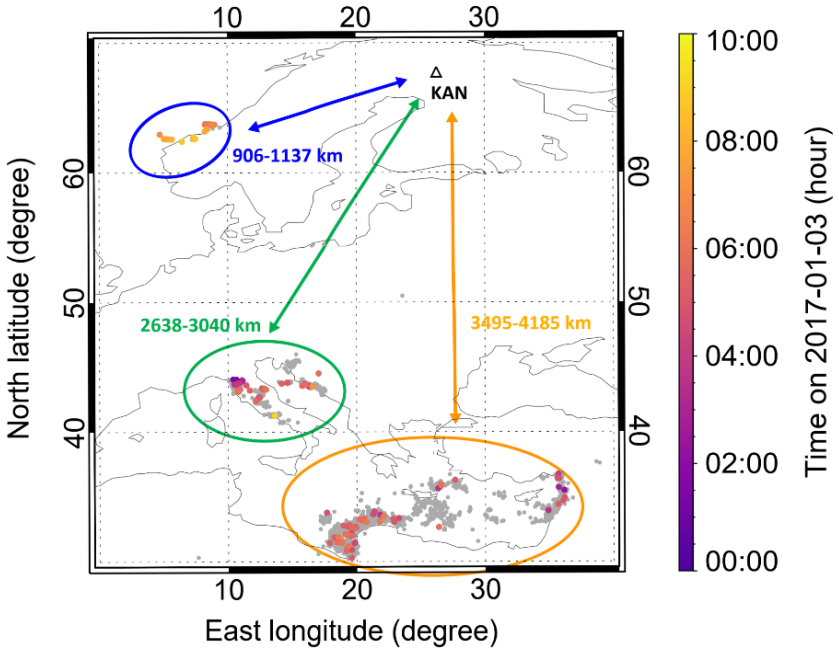

Fig. 8. The locations of lightning discharges from the consolidated list of EUCLID and WWLLN detections (in grey) are shown, with the source lightning discharges for echo trains in color coded by the time of their occurrence. The colors correspond to the time of lightning occurrence. The colored ovals mark three separated areas with the lightning activity (Northern thunderstorm – blue, Central Mediterranean – green, and Eastern and African Mediterranean – orange).

Kolmašová, I., **Santolík**, O. & Manninen, J. (2024), Whistler echo trains triggered by energetic winter lightning. *Nature Communications 15*, 7166. https://doi.org/10.1038/s41467-024-51684-0

Linzmayer, V., Němec, F., **Santolík, O.**, & **Kolmašová, I.** (2024). Lightning-induced energetic electron precipitation observed in long-term DEMETER spacecraft measurements. *Journal of Geophysical Research: Space Physics, 129*, e2024JA032713. https://doi.org/10.1029/2024JA032713

Sub-MeV Electron Precipitation Driven by EMIC Waves through Nonlinear Fractional Resonances

Electromagnetic ion cyclotron waves in the Earth's outer radiation belt drive rapid electron losses through wave-particle interactions. The precipitating electron flux can be high in the hundreds of keV energy range, well below the typical minimum resonance energy. One of the proposed explanations relies on nonresonant scattering, which causes pitch-angle diffusion

away from the fundamental cyclotron resonance. Here we propose the fractional sub-cyclotron resonance, a second-order nonlinear effect that scatters particles at resonance order n = 1/2, as an alternate explanation. Using test-particle simulations, we evaluate the precipitation ratios of sub-MeV electrons for wave packets with various shapes, amplitudes, and wave normal angles. We show that the nonlinear sub-cyclotron scattering produces larger ratios than the non-resonant scattering when the wave amplitude reaches sufficiently large values. The ELFIN CubeSats detected several events with precipitation ratio patterns matching our simulation, demonstrating the importance of sub-cyclotron resonances during intense precipitation events.

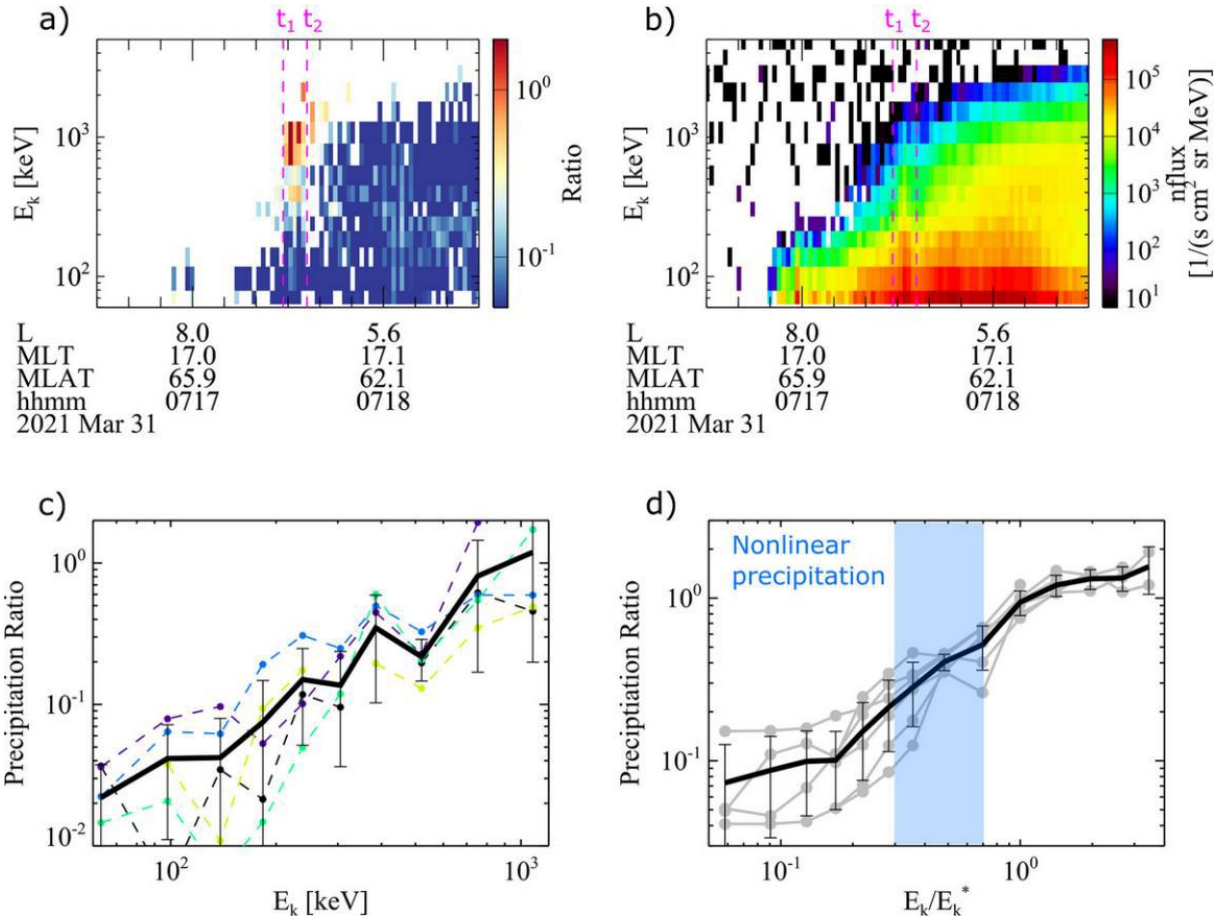

Fig. 9. Electron precipitation detected by the ELFIN CubeSats. (a) Precipitation ratios detected by ELFIN-A on 31 March 2021 in the northern hemisphere, with a typical EMIC-driven precipitation pattern shown between t1 = 07:17:30 and t2 = 07:17:33 (dashed magenta lines). (b) Trapped electron number flux. (c) Line plots of precipitation ratios between t1 and t2, with each dashed colored line representing a single half-spin and the thick black line showing the average with standard deviations as error bars. (d) Statistical precipitation ratios in selected events plotted against normalized energy. Gray lines represent averages over individual events; the black line is the sample average with error bars showing the standard deviations. The light blue area highlights the energy range where the strongest effects from the n = 1/2 nonlinear resonance are expected.

Hanzelka, M., Li, W., Qin, M.,Capannolo, L., Shen, X., Ma, Q., Gan, L., & Angelopoulos, V. (2024), Sub-MeV Electron Precipitation Driven by EMIC Waves through Nonlinear Fractional Resonances, *Geophysical Research Letters, 51*, e2023GL107355. https://doi.org/10.1029/2023GL107355

Radial Variations in Solar Type III Radio Bursts

Type III radio bursts are generated by electron beams accelerated at reconnection sites in the corona. This study, utilizing data from the Parker Solar Probe's first 17 encounters, closely examines these bursts down to 13 solar radii. A focal point of our analysis is the near-radial alignment (within 5°) of the Parker Solar Probe, STEREO-A, and Wind spacecraft relative to the Sun. This alignment, facilitating simultaneous observations of 52 and 27 bursts by STEREO-A and Wind respectively, allows for a detailed differentiation of radial and longitudinal burst variations. Our observations reveal no significant radial variations in electron beam speeds, radio fluxes, or exponential decay times for events below 50 solar radii. In contrast, closer to the Sun we noted a decrease in beam speeds and radio fluxes. This suggests potential effects of radio beaming or alterations in radio source sizes in this region. Importantly, our results underscore the necessity of considering spacecraft distance in multi-spacecraft observations for accurate radio burst analysis. A critical threshold of 50 solar radii emerges, beyond which beaming effects and changes in beam speeds and radio fluxes become significant. Furthermore, the consistent decay times across varying radial distances point toward a stable trend extending from 13 solar radii into the inner heliosphere. Our statistical results provide valuable insights into the propagation mechanisms of type III radio bursts, particularly highlighting the role of scattering near the radio source when the frequency aligns with the local electron plasma frequency.

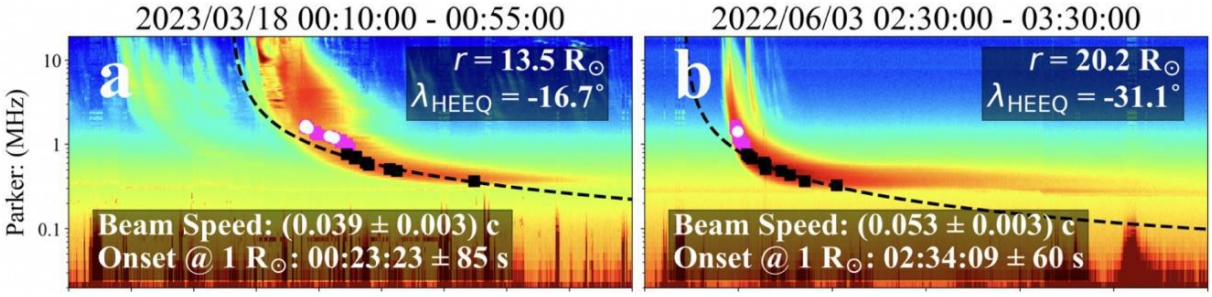

Fig. 10. Radio measurements from the Parker Solar Probe (panels (a)–(b) on 2023 March 18 between 00:10 and 00:55 UT (Case #1, left), on 2022 June 3 between 02:30 and 03:30 UT. Panels mark peak fluxes within our targeted frequency range using squares. Black squares denote peak fluxes used to calculate electron beam speeds based on the empirical density model, with fitted electron beams shown by black dashed lines and the computed speeds and onset times at 1 Rs noted in each panel. Magenta squares highlight peak fluxes outside our propagation analysis frequency range. White circles indicate peak fluxes when the wave vector azimuth was within 5°, implying minimal radio propagation variation and suggesting that the type III bursts originated near the line connecting the Parker Solar Probe and the Sun.

Krupar, V., Kruparova, O., Szabo, A., Wilson, L. B., Nemec, F., **Santolik, O**., Pulupa, M., Issautier, K., Bale, S. D., & Maksimovic, M. (2024). Radial Variations in Solar Type III Radio Bursts, *Astrophys. J. Lett.*, 967 (2): Art. No. L32. https://doi.org/10.3847/2041-8213/ad4be7

Boldú, J. J., Graham, D. B., Morooka, M., André, M., Khotyaintsev, Y. V., Dimmock, A., **Píša, D.**, **Souček, J.** et al. (2024). Ion-Acoustic Waves Associated With Interplanetary Shocks, *Geophysical Research Letters*, 51, 16, e2024GL109956. https://doi.org/10.1029/2024GL109956

Polarization Analysis of Type III Langmuir/Z-mode Waves with Coherent Magnetic Component Observations by Solar Orbiter

Observations from the Solar Orbiter spacecraft provide unique insights into the interaction between electron beams and the plasma background in the source regions of type III radio emissions. We analyzed this interaction by examining the high-frequency electric and magnetic components of in situ wave measurements, focusing on their polarization properties. Using electron data from onboard instruments, we modeled the electron velocity distribution function and numerically solved the dispersion relation. We compared the predicted polarization of the electric and magnetic components with the observations. Our findings re consistent with propagation in the Langmuir/Zmode at an oblique wave vector. We explain the magnetic component and transverse polarization by the presence of small density fluctuations, without the need for mode conversion.

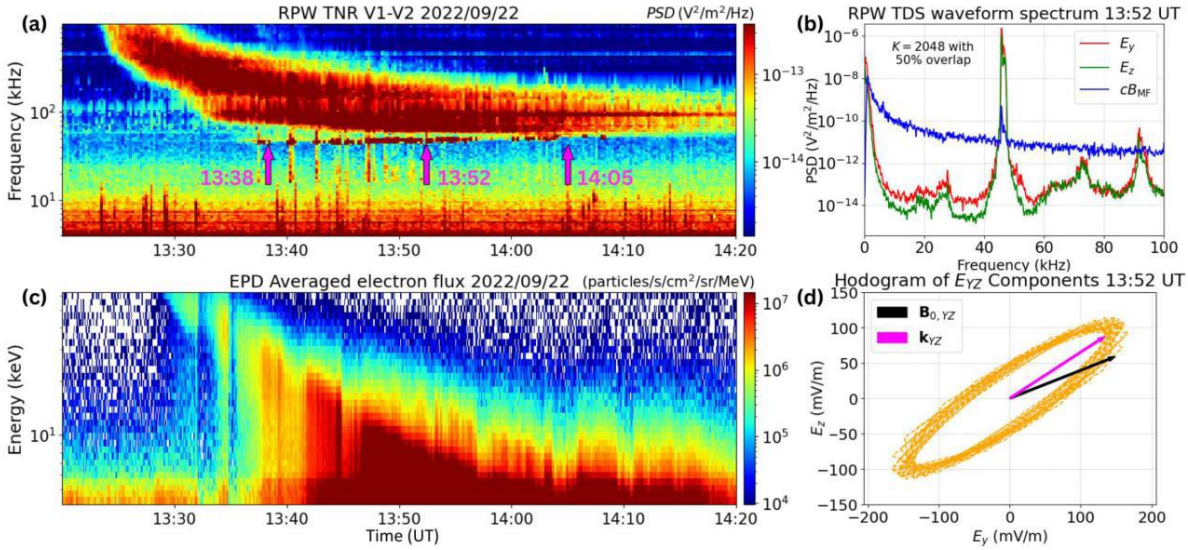

Fig. 11. Overview of the type III radio emission on 2022 September 22. (a) The radio emission and Langmuir waves, highlighting three specific timestamps. At 13:38 UT and 14:05 UT, we analyze the electron data, while 13:52 UT marks the strongest Langmuir wave observations. (b) Spectrum of the observed waveform at 13:52 UT, including a coherent high-frequency signal from the search coil magnetometer. (c) The averaged electron Eux from the STEP instrument. (d) A hodogram of the strongest electric field observations (100 samples), with arrows marking the projection of the ambient magnetic field (black) and the predicted wave vector directions.

A Dataset of Lower Band Whistler Mode Chorus and Exohiss with Instrumental Noise Thresholds

In this work, we presented a large database of natural electromagnetic emissions of lower band whistler mode chorus and exohiss within the Earth's magnetosphere. It is based on more than 124 million selected survey measurements of magnetic fluctuations, recorded between 2001 and 2020 by the two NASA Van Allen Probes and four ESA Cluster spacecraft. The database provides a comprehensive view of amplitudes of these important electromagnetic emissions in the audible frequency range. We carefully conditioned the data to minimize the influence of

instrumental artefacts. We also removed all data points which might have be contaminated by instrumental noise using a newly developed method to define detection thresholds as a function of frequency, time, and instrument settings. The database can serve as a valuable resource for a broad range of scientists studying space weather, magnetospheric physics, and radiation belt dynamics.

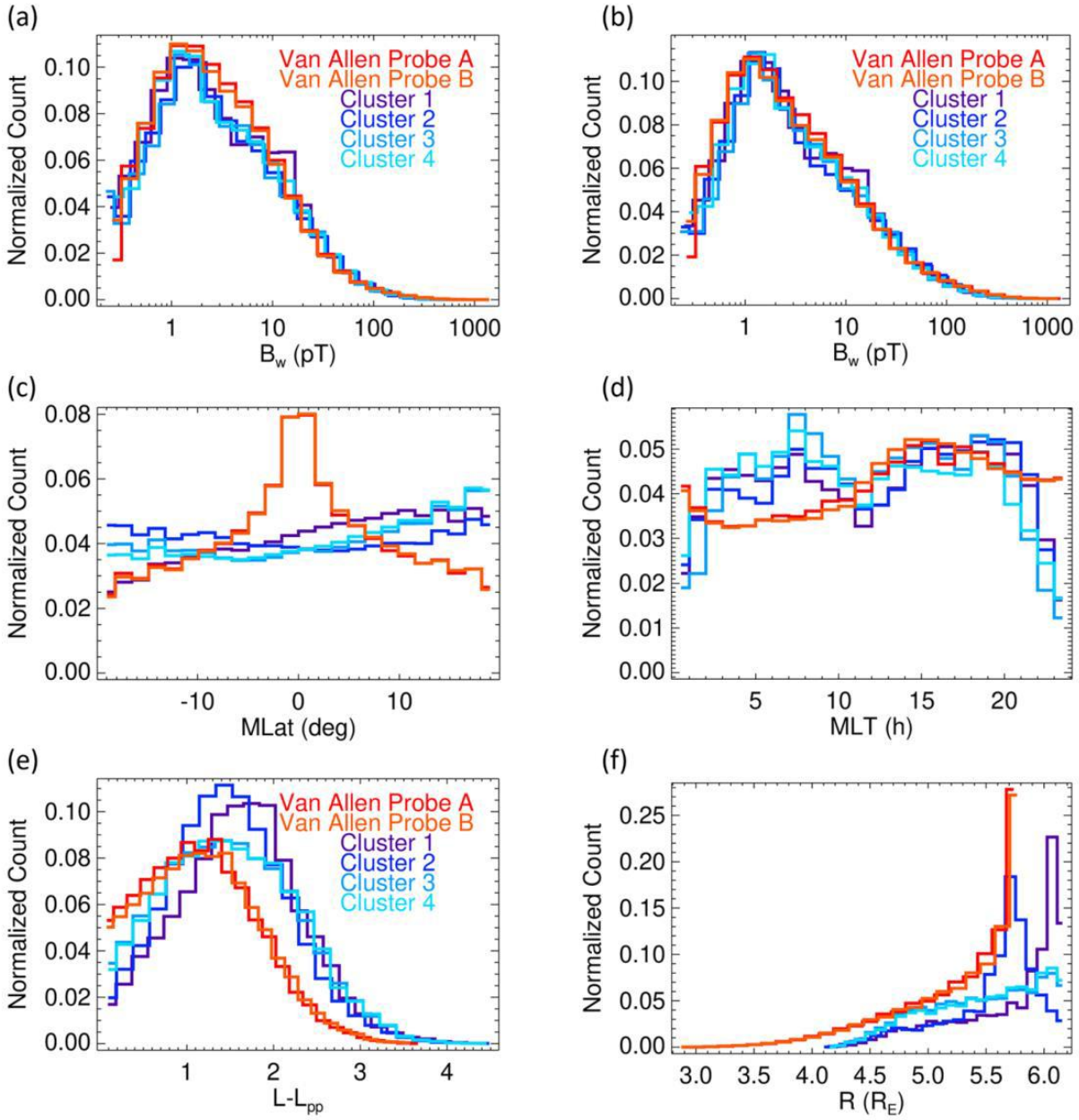

Fig. 12. Distributions root-mean-square amplitudes and spatial coverage of overlapping measurements of lower-band chorus and exohiss. Color coded distributions are given for datasets from Table 3 from the paper. (a) Distributions of root-mean-square amplitudes Bw, (b) the same but for the restricted datasets on the morning side with magnetic local time of 0–12 h, (c) distributions of magnetic latitudes for the datasets from panel a, (d) distributions of magnetic local time, (e) distributions of equatorial distances from the model plasmapause, (f) distributions of radial distances, all for the datasets from panel a. Histograms in 25 logarithmic bins are always normalized by the total number of measurements.

Santolík, O., Kolmašová, I., Taubenschuss, U., Hanzelka, M., & Hartley, D.P. (2025). A Dataset of Lower Band Whistler Mode Chorus and Exohiss with Instrumental Noise Thresholds. Sci. Data, 12 (1), 1265. https://doi.org/10.1038/s41597-025-05531-6
Němec, F., **Santolik**, O., Albert, J. M. (2025). VLF Transmitter Signals Observed by the Cluster Spacecraft Over a Wide Range of Latitudes, *J. Geophys. Res. Space Physics*, 130, e2024JA033621, https://doi.org/10.1029/2024JA033621

Localization of the Cluster satellites in the geospace environment

The geometry of the terrestrial magnetized environment, or geospace, varies widely in space and time due to the Earth's magnetic field interactions with the interplanetary medium. A spacecraft's location in geospace is only approximately determined by its coordinates since the environment is inhomogeneous, with distinct physical processes occurring in different regions. Knowing the location in the geospace offers a strong support for data analysis. This paper introduced a new dataset, Geospace Region and Magnetospheric Boundary identification (GRMB), which provides labelled positions for each Cluster spacecraft over the whole mission, with respect to the local environment. This continuous labelling is based on manual selection, supported by browsing 44 different Cluster data products. The GRMB dataset includes 15 labels spanning from the plasmasphere to solar wind regions. Its consistency was validated over 7 years against reference lists and by the physical properties of the GRMB regions. Over those years, Cluster spent a similar proportion of the time (≈15%) in the regions labelled lobe, plasmasheet, plasmasheet transition region, magnetosheath and solar wind.

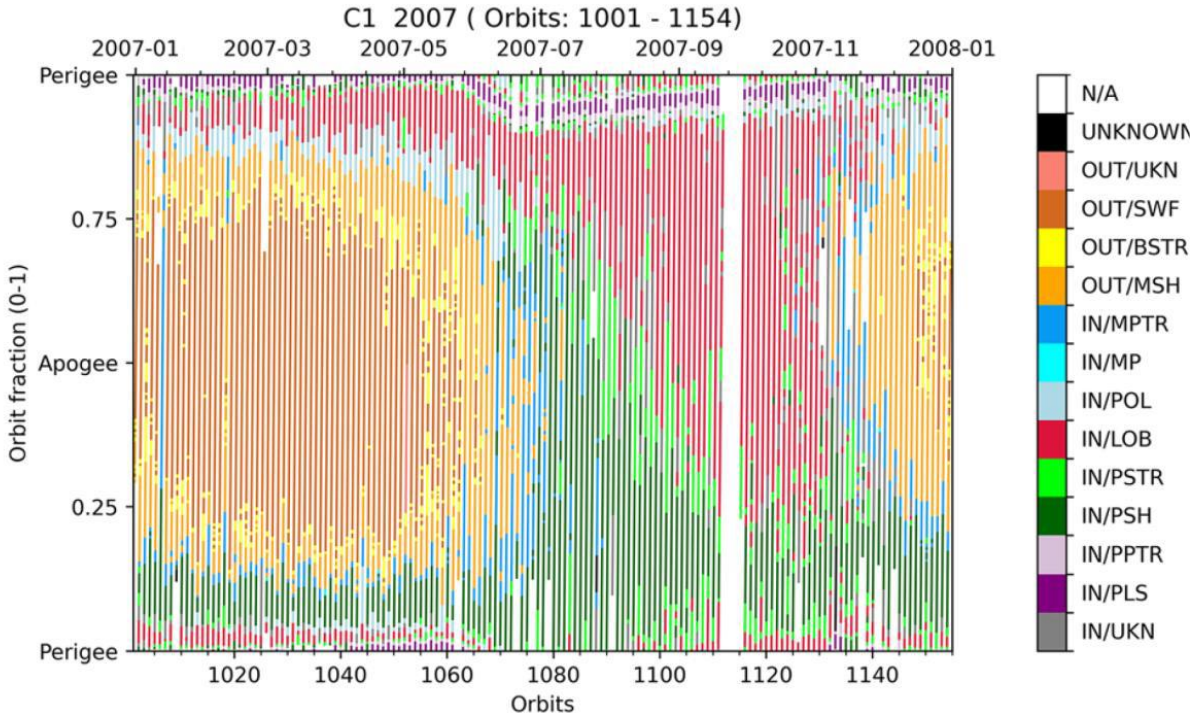

Fig. 13. Location of the Cluster-1 spacecraft in year 2007 (orbits 1001 to 1154) according to the GRMB dataset.

Grison, B., Darrouzet, F., Maggiolo, R., **Hajoš, M., Dvořák, M., Švanda, M., Ječábková, A.**, Graham, M., Taylor, G.T., Herment, D., Masson, A., **Souček, J., Santolík, O.**, & De Keyser, J. (2025). Localization of the Cluster satellites in the geospace environment. *Scientific Data* 12, 327. https://doi.org/10.1038/s41597-025-04639-z

Nonlinear acceleration of ultrarelativistic electrons in the outer radiation belt disrupted by transverse wave modulations

Whistler-mode waves scatter ultrarelativistic electrons in the radiation belts and accelerate them through resonant interactions. In simplified models, nonlinear phase trapping by high-amplitude waves can increase electron energy by several MeV within seconds. However, the acceleration rate in realistic wave packets is slower due to small-scale wave field structures

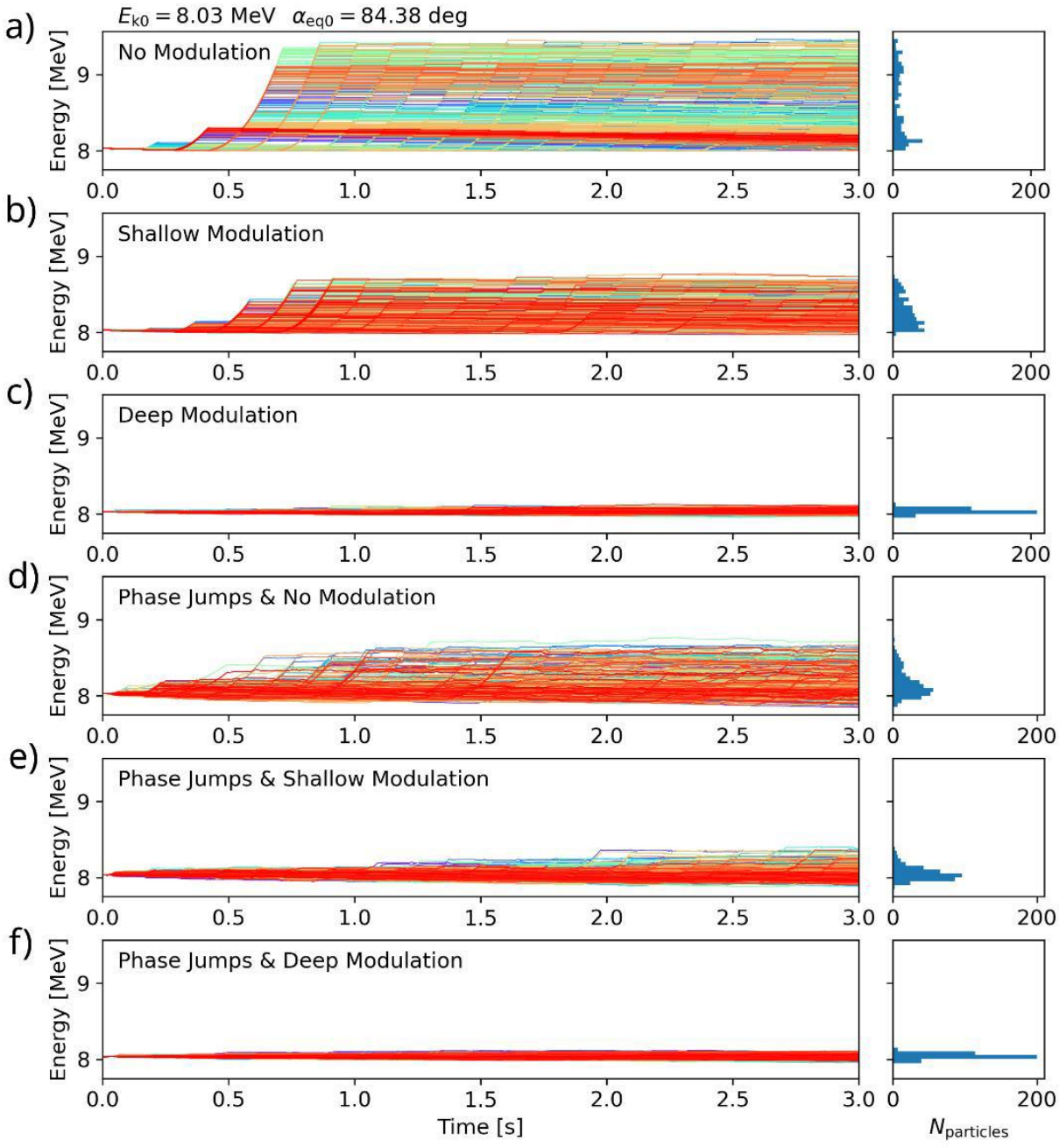

Fig. 14. Evolution of electron energy for initial energy and pitch angle of 8.03 MeV and 84.38°. The first column shows individual electron trajectories color-coded by initial gyrophase, while the second column presents energy histograms at t = 3 s. (a–c). Various modulation depths without phase jumps at amplitude minima. (d–f) Wave models with phase jumps.

reducing trapping efficiency. While previous studies focused on short field-aligned amplitude modulations and phase jumps, we examine the effects of transverse modulations, which have been observed to reach scales comparable to ultrarelativistic electron gyroradii. Using test-particle simulations, we demonstrated that these modulations disrupt the acceleration process. Our numerical results suggest that nonlinear trapping plays a negligible role in accelerating electrons above a certain energy limit, reinforcing the diffusive nature of wave-driven electron transport at multi-MeV energies. Unlike field- aligned structures, transverse phase incoherence modifies the effective wave spectrum and allows for resonance, making amplitude modulations a necessary component for suppression of acceleration.

Hanzelka, M., Shprits, Y. Y., & **Santolík, O.** (2025). Nonlinear acceleration of ultrarelativistic electrons in the outer radiation belt disrupted by transverse wave modulations. *Geophysical Research Letters*, 52, e2025GL116883. https://doi.org/10.1029/2025GL116883
Ma, Q., Li, W., Bortnik, J., **Hanzelka, M.**, Gan, L., Artemyev, A. V., & Shen, X.-C. (2025). Diffusive and nonlinear scattering of ring current protons by electromagnetic ion cyclotron waves in the Earth's inner magnetosphere. *J. Geophys. Res. Space Physics*, 130, e2025JA034078. https://doi.org/10.1029/2025JA034078.

Effects of fine spectral structure of chorus emissions on nonlinear scattering and acceleration of radiation belt electrons

Whistler-mode chorus waves play a crucial role in accelerating electrons in Earth's outer radiation belt to relativistic and ultrarelativistic energies. While this electron evolution is typically modeled using a diffusion approximation for scattering, high-amplitude chorus waves induce nonlinear resonant effects that challenge this approach on short time scales. The long-term influence of these nonlinear interactions on radiation belt dynamics remains an unresolved issue. Recent simplified models suggest rapid nonlinear acceleration to ultrarelativistic energies, with formation of butterfly distributions during parallel wave propagation. In this study, we introduced a novel numerical approach based on Liouville phase space density mapping to investigate nonlinear scattering by high-amplitude waves over extended periods (minutes and beyond). We use a numerical wave field model of lower-band chorus risers that includes realistic fine-spectral features including subpacket modulations, phase decoherence, and jumps in wave normal angle. By incorporating these detailed spectral characteristics of the waves, we demonstrate that the rapid acceleration occurs across a broader pitch-angle range, forming a flat-top distribution. Similar effect is observed as the repetition period of chorus elements becomes shorter, with the additional effect of increased electron precipitation due to transition from bursty to continuous flux profiles in the loss cone. These findings highlight the importance of incorporating nonlinear effects and fine-scale wave properties in the future development of high energy electron models for the outer radiation belt.

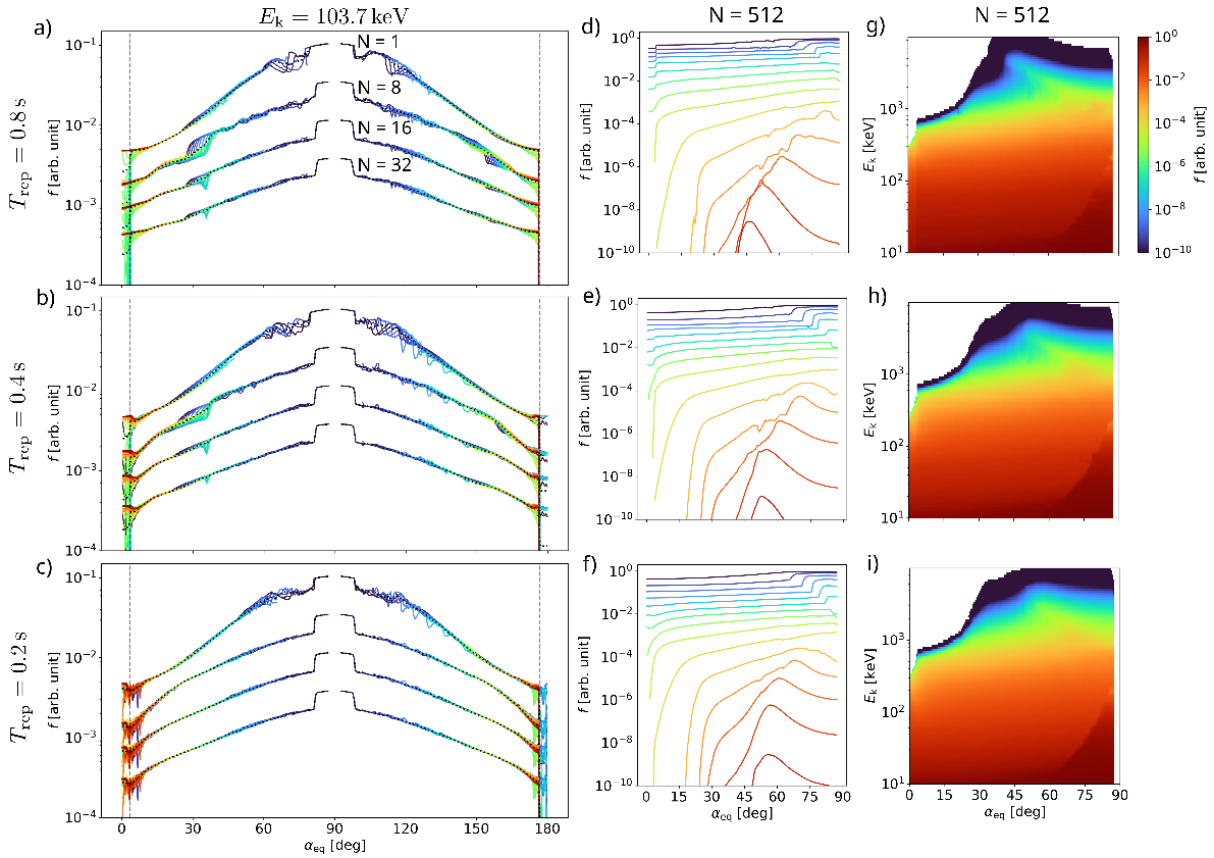

Fig. 15. The effects of chorus repetition period Trep on the phase sp.ace density (PSD) evolution, with each row corresponding to one of the three values 0.8 s, 0.4 s, and 0.2 s. In all three cases, the wave field is parametrized by 2σω = 0 Ωe0, 2σθ = 0°. The first column (panels a–c) shows the state of local PADs at four different time points given by the number of cycles N = {1, 8, 16, 32}; the energy value is always the same, Ek = 104.7 keV. As the number of cycles increases, the PSD values are multiplied by 1/3 each time to fit all lines into one plot without major overlaps. The second column (panels d–f) shows the PADs at N = 512 across several energy levels coded by color, with the same legend as in Figure 5. The dashed gray lines in panels a–f represent the equatorial loss cone. The third column (panels g–i) shows the two-dimensional PSD distribution in energies and equatorial pitch angles as a heat map.

Hanzelka, M., Shprits, Y., Wang, D., Haas, B., **Santolík, O.**, & Gan, L. (2025). Effects of fine spectral structure of chorus emissions on nonlinear scattering and acceleration of radiation belt electrons. J. Geophys. Res. Space Physics, 130(4), e2024JA033382. https://doi.org/10.1029/e2024JA033382

Gan, L., Li, W., Albert, J., **Hanzelka, M.**, Ma, Q., & Artemyev, A. (2025). Inhomogeneity Ratio for Nearly Field-Aligned Electrons Interacting With Whistler-Mode Waves J. Geophys. Res. Space Phys., 129(10), e2024JA032554. https://doi.org/10.1029/2024JA032554

A Global Map of Average Electron Densities in the Magnetosphere of Saturn

Measurements from the Cassini Radio and Plasma Wave Science (RPWS) experiment obtained during the entire orbital phase of the Cassini mission around Saturn (13.2 years) are processed into a meridional map of plasma densities, comprising the innermost region of the ring ionosphere, the Enceladus plasma torus, and the outer magnetosphere, up to a dipole L-shell of

30. We combined data from RPWS wave observations, such as whistler-mode waves and upper hybrid electrostatic emissions, and from the RPWS Langmuir probe when operated in the proxy mode, providing an estimate for the spacecraft potential. In the region between dipole L-shells of 2.4 and 30, observed electron densities are described by an analytic model that fits two functions, one for the water group ions and one for the protons, to observed densities across latitude on each magnetic field line. The derived electron density profiles are then augmented by a model for the cold core electron temperature as a function of L-shell to obtain a meridional map of the electrostatic potential of the ambipolar electric field. The potential is extrapolated to the inner region of the rings, i.e., to below L = 2.4, to solve for the distribution of electron density in the ring ionosphere. A solution is based on a diffusive equilibrium model for the electrons and two ion species, and on observations from Cassini along the Saturn Orbit Insertion trajectory. A combination of analytic and diffusive equilibrium results finally yields an average global picture for the distribution of electron density in Saturn's magnetosphere.

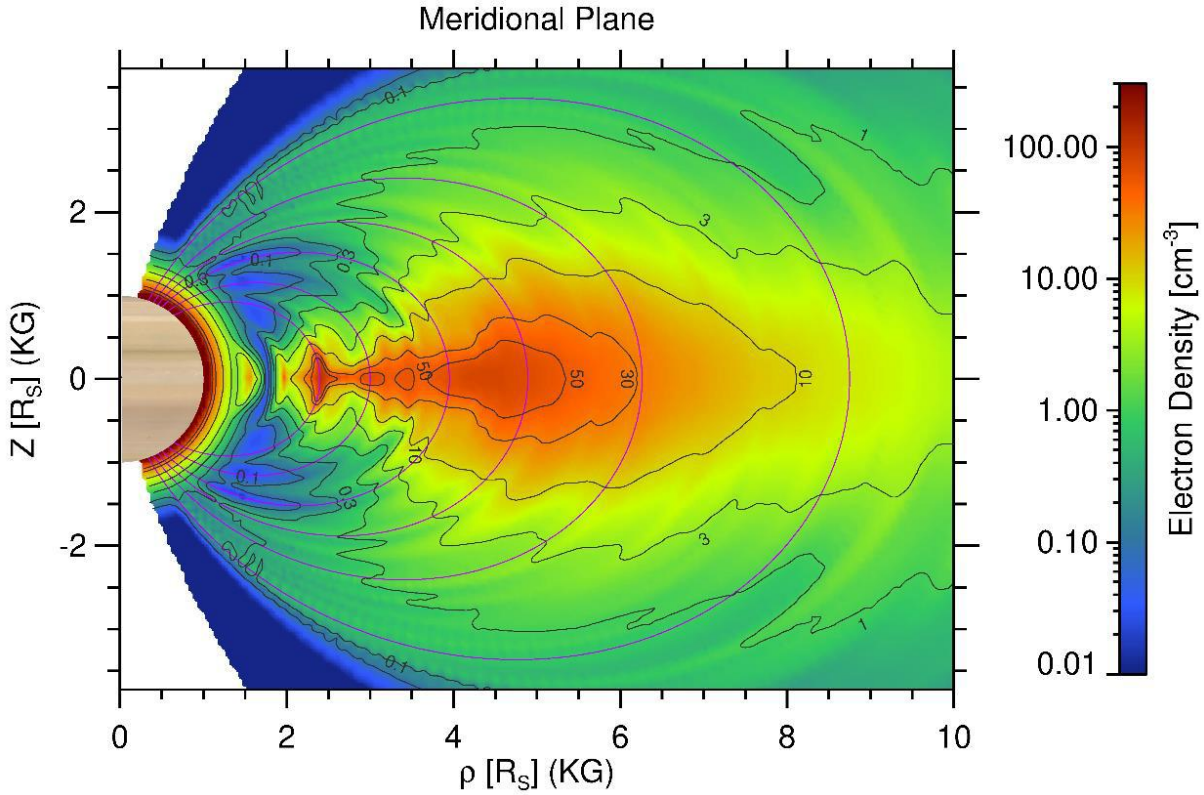

Fig. 16. Meridional distribution of electron density in the inner magnetosphere of Saturn from the model of Taubenschuss et al. (2025). Prominent features are the Enceladus plasma torus, stretching between equatorial distances ρ of 3 - 10, density peaks connected to the rings (inside ρ = 3 Rs), a plasma void above the B ring, and a high-latitude plasmapause. Planetary magnetic dipole field lines are overplotted in purple color.

Taubenschuss, U., O. Santolík, D. Píša, M. Imai, G. Fischer, S. Wu, M. W. Morooka, & W. S. Kurth (2025). A Global Map of Average Electron Densities in the Magnetosphere of Saturn, J. Geophys. Res. Space Physics, 130, e2025JA034007. https://doi.org/10.1029/2025JA034007
Fischer, G., **M. Imai, U. Taubenschuss, D. Píša**, and W. S. Kurth (2025). The radio wave polarization of Saturn lightning observed by Cassini, J. Geophys. Res. Space Physics, 130, e2024JA033560, https://doi.org/10.1029/2024JA033560

Solar cycle signatures in lightning activity

Cross-correlation between annual lightning/thunder frequency and solar activity was examined globally for the period 2009-2022 using World Wide Lightning detection network. The results do not support previous works indicating that cosmic ray intensity (anticorrelated with solar activity) should be in phase with the global lightning frequency. We do not exclude that cosmic rays help ignite lightning in developed thunderclouds and that energetic particles precipitating from the magnetosphere affect the frequency of lightning in the region of the South Atlantic Anomaly of the geomagnetic field.

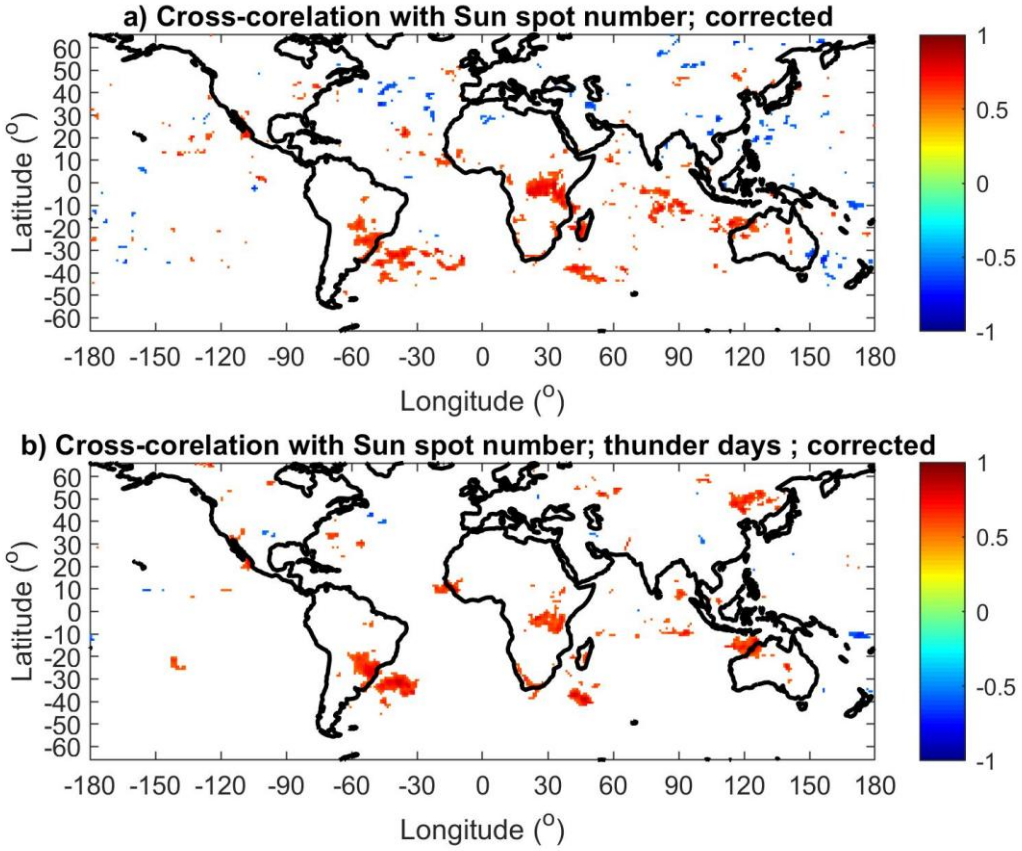

Fig. 17. Cross-correlation coefficients between yearly Sunspot Number (SSN) and number of lightning strokes in 1°x1° bins (color-coded). (b) Cross-correlation coefficients between yearly SSN and yearly thunder days in 1°x1° bins. Only statistically significant cross-correlation coefficients are displayed (p<0.05). If the cosmic rays were in phase with the frequency of lightning, distinct blue areas would appear on the map.

Chum, J., Langer, R., **Kolmašová, I., Lhotka, O., Rusz, J.**, Strhárský, I. (2024): Solar cycle signatures in lightning activity, *Atmospheric Chemistry and Physics*, 24, 9119–9130, https://doi.org/10.5194/acp-24-9119-2024.

Impact of storm "Zyprian" on the middle and upper atmosphere observed in Central Europe

Mesoscale convective systems are effective sources of atmospheric disturbances, which can propagate through the atmosphere up to the F region ionosphere and significantly affect the

state of the atmosphere and ionosphere. The extratropical cyclone Zyprian formed in early July 2021 and its cold front passed from west over the whole Europe, accompanied by strong convective precipitation and thunderstorms. The thunderstorm activity was recorded by microbarographs as infrasonic and gravity waves. A change of jet stream position and important increase of humidity over thunderstorm areas were observed in the stratosphere. An extraordinary stratification occurred in the ionosphere. An increase of wave activity was observed on ionograms and by VLF data. Digisonde directograms and SKY maps displayed strong and rapid changes in horizontal motions of ionospheric plasmas. The remarkable increase of variability at ionospheric heights can be related to the cyclone Zyprian, because the geomagnetic activity was low and solar activity stable.

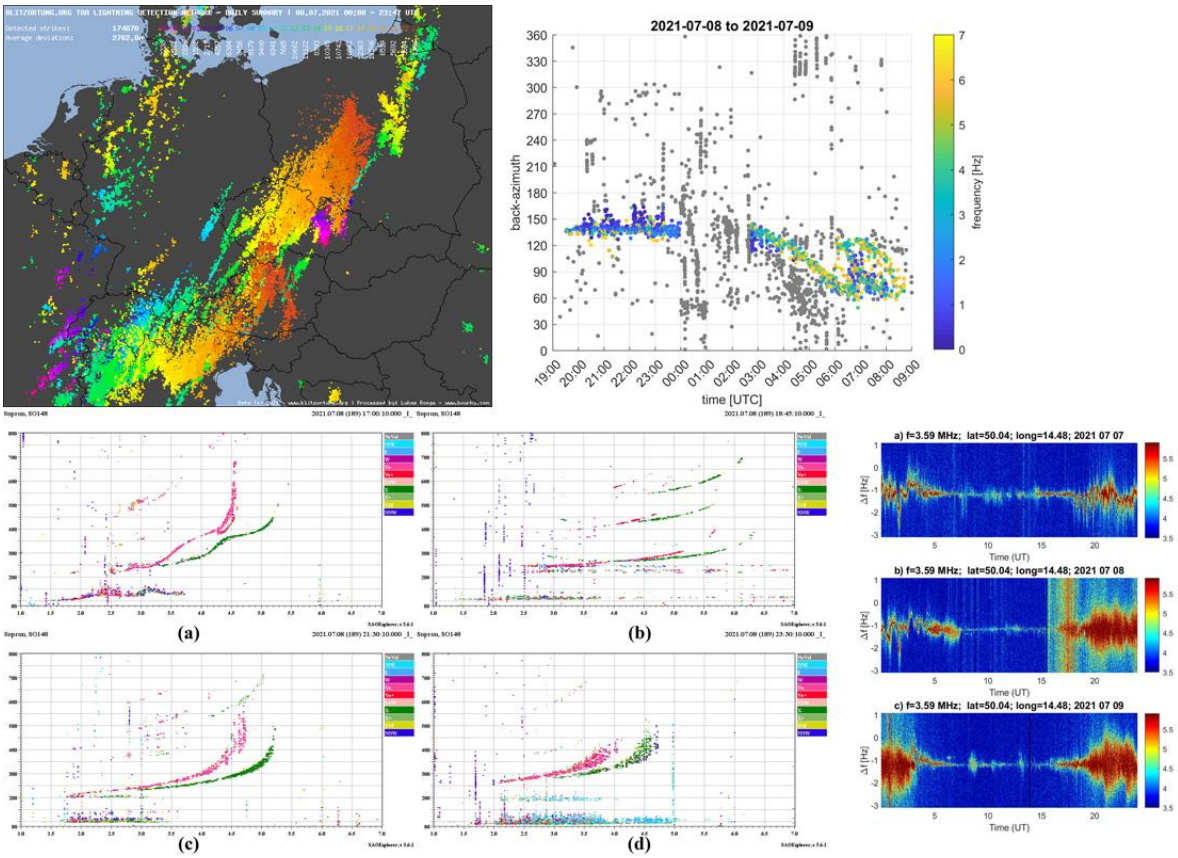

Fig. 18. Distribution of lightning activity over Central Europe (top left panel) on 8 July 2021. Recording of infrasound at 22:00-05.00 UT (top right panel) related to motion of convective thunderstorm system. Ionograms measured at station Sopron (left bottom panel) with irregularities of reflections, particularly in F region. Doppler shift record in Czechia at 3.59 MHz on 7-9 July 2021 (bottom right panel) with clear amplification of signal immediately after passing the convective system.

Koucká Knížová, P., Potužníková, K., Podolská, K., Šindelářová, T., Bozóki, T., Setvák, M., Pásztor, M., Szárnya, C., **Mošna, Z., Kouba, D**., **Chum, J.** et al. (2024). Impacts of storm "Zyprian" on middle and upper atmosphere observed from Central European stations. Remote Sensing, 16, 4338. https://doi.org/10.3390/rs16224338

F30 is the best solar activity proxy for long-term TEC investigations

To study ionospheric climate, to model the ionosphere and to investigate its long-term changes and trends, solar activity proxies/indices have been used, because long and homogeneous data series of solar ionizing flux are not available. In the Report 2022-2023 we reported F30 to be the best solar index for analyzing midlatitudinal foF2. Here we analyze the homogeneous series JPL-35 of global total electron content (TEC) data for 1994-2014 for selection of the optimum solar activity proxy for TEC. Six solar activity proxies, F10.7, sunspot numbers, F30, Mg II, He II, and solar H Lyman-a flux are used and four criteria are applied: 1. Percentage of total variance of TEC described by solar activity proxy should be the largest one. 2. The standard error of trend slope/coefficient D should be the smallest one. 3. Percentage of total variance of TEC residuals ($TEC_{obs} - TEC_{mod}$) described by trend with the given solar proxy should be the largest one. 4. The average of absolute values of differences between observed and model (with solar proxy) TEC (TEC residuals) should be the smallest one. While the first two criteria do not reveal significant differences between most solar proxies, the third and fourth criteria clearly favor again F30, **which means change of paradigm**. On the other hand, preliminary results for foE indicate rather F10.7 as the best solar proxy. The difference between optimum solar proxies for foF2 and TEC versus foE is related to different parts of solar EUV spectrum responsible for their behavior.
Using global IGS TEC maps for 2003-2023, long-term trends of TEC were calculated. As Fig. 14 illustrates, these trends are insignificantly small except for low latitudes, where they are globally large and significant in two longitudinal regions and insignificant and small in two other regions.

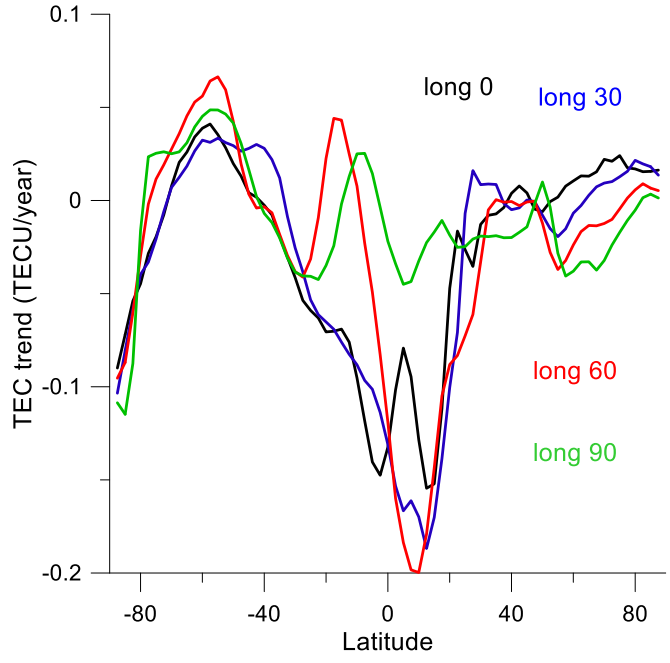

Fig. 19. Latitudinal dependence of TEC trends (TECU/year) for longitudinal belts centered at 0º, 30º, 60º and 90º, latitudes 87.5ºS-87.5 N.

Urbar, J., Lastovicka, J. (2025). Global long-term trends in the total electron content. Annales Geophysicae, 43 (1), 67-72, https:doi.org/10.5194/angeo-43-67-2025.

Lastovicka, J. (2024). Dependence of long-term trends in foF2 at middle latitudes on different solar activity proxies. Advances in Space Research, 73 (1), 685-689, https://doi.org/10.1016/j.asr.2023.09.047.

Impact of moderate geomagnetic storm on ionized as well as neutral upper atmosphere as observed by ICON satellite

A response is presented of the ionized as well as neutral components of Earth's upper atmosphere to the 14 January 2022 moderate geomagnetic storm using ICON satellite observations. Global-scale analysis of ion density and thermospheric wind speed as a function of latitude and longitude covering 160-600 km altitude range provides descriptive illustrations of storm-time responses of different layers of the ionosphere. The storm induced disturbances at almost all altitudes considered in the study and the Hunga eruption caused high wind variations at lower altitudes (160-200 km). We also considered the effects of a co-incident Hunga Tonga volcanic eruption, while our focus remains on the ionosphere-thermosphere responses to the storm. Our analyses depicted strong equatorial and low latitude ion density enhancement on 14-01-2022 (12:01-23:59 LT) across almost all longitudes, which corresponds to the times after the sudden storm commencement (SSC). Compared to 13-14 January 2022 (00:00-12:00 LT), a high ion density is observed on 15-01-2022 (00:00-12:00 LT), especially over 0-200^{o} E. This ion density enhancement persists on 16-01-2022 (at all times of the day) with a similar scenario seen on 15-01-2022. Storm-enhanced wind speed irregularity decreases relatively with an increase in altitude. Ion density is higher in 12:01-23:59 LT than in 00:00-12:00 LT during all days considered. On 15-01-2022 (12:01-23:59 LT), fluctuating structure of ion density is observed in 0-200^{o} E over the dip equator region which was found to be associated with the Hunga eruption. Generally, the moderate geomagnetic storm caused a positive ionospheric storm, which enhanced ion density and triggered turbulence in the wind dynamics.

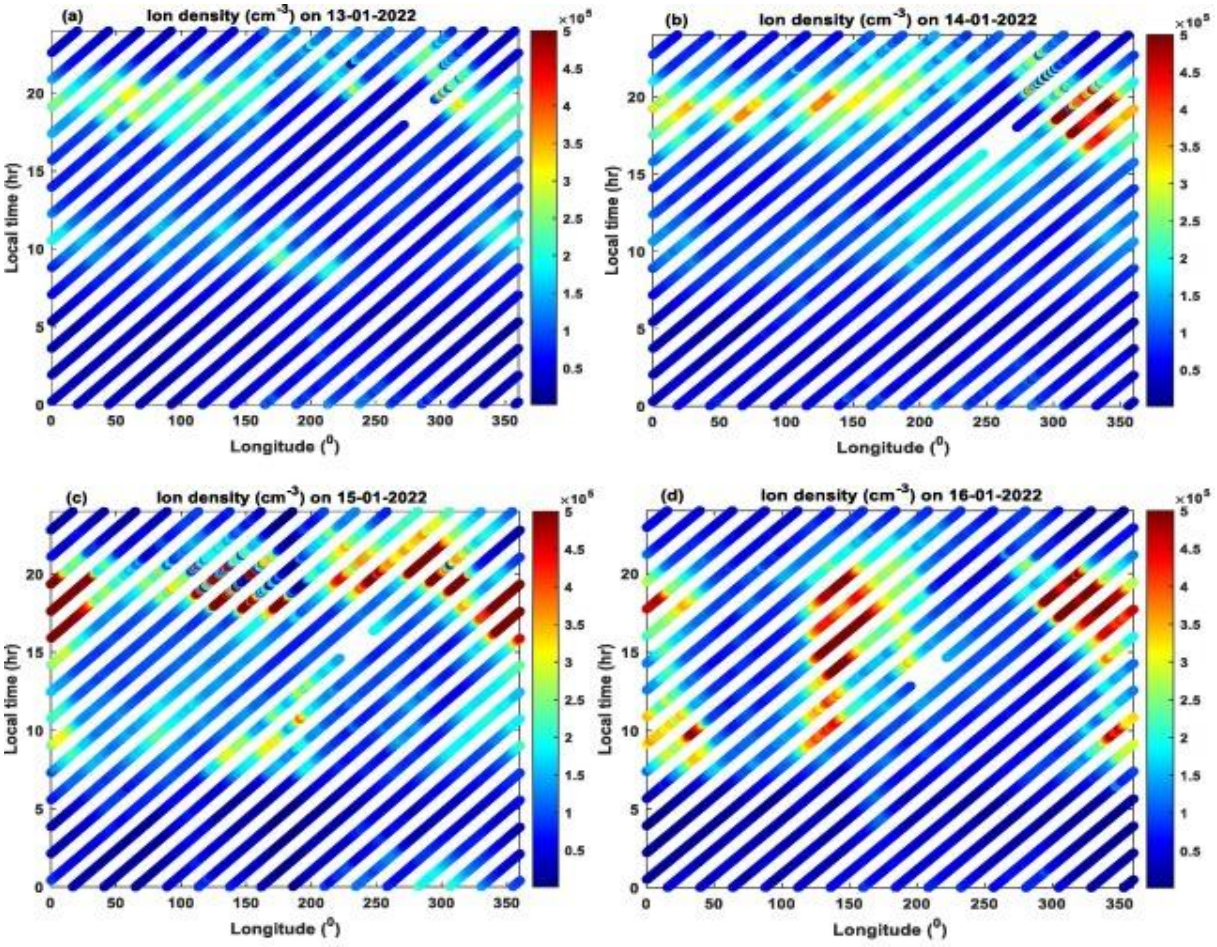

Fig. 20. Ion density observations of ICON satellite as a function of longitude and local time from 13 to 16 January 2022.

Marew, H., Aksonova, K., Lastovicka, J., Chum, J., Mosna, Z., Urbar, J., Kouba, D., Koucka Knizova, P., Rusz, J., Rejfek, L., Base, J. (2025). Ionosphere-thermosphere response to the January 14, 2022 moderate storm: ICON satellite observations. Advances in Space Research, 76 (4), 2315-2327, https://doi.org/ 10.1016/j.asr.2025.05.088.

Astronomical Institute of the Czech Academy of Sciences (ASU CAS):

Black hole X-ray binaries

Black hole X-ray binaries are known to be highly variable objects exhibiting different accretion states with variable spectral and timing properties. The first investigation of how the X-ray polarization properties of a source evolve with the spectral state was enabled by an extraordinarily bright X-ray outburst of Swift J1727.8–1613, discovered in August 2023. The 2–8 keV polarization degree measured by the Imaging X-ray Polarimetry Explorer (IXPE) was about 4% in the hard state, when the X-ray emission is dominated by the Comptonised emission from a hot corona of relativistic electrons. Based on our observational proposal, IXPE observed the source in February 2024 in the soft state, with the X-ray flux dominated by the thermal accretion disk emission. The polarization degree dropped dramatically to $\lesssim$1%, which for the first time unambiguously proved that the measured X-ray polarization is largely sensitive to the accretion state and the polarization fraction is significantly higher in the hard state when the X-ray emission is dominated by upscattered radiation in the X-ray corona. The combined measurements in the hard and soft state allowed us to constrain the inclination of the accretion disc to be around 40 degrees.

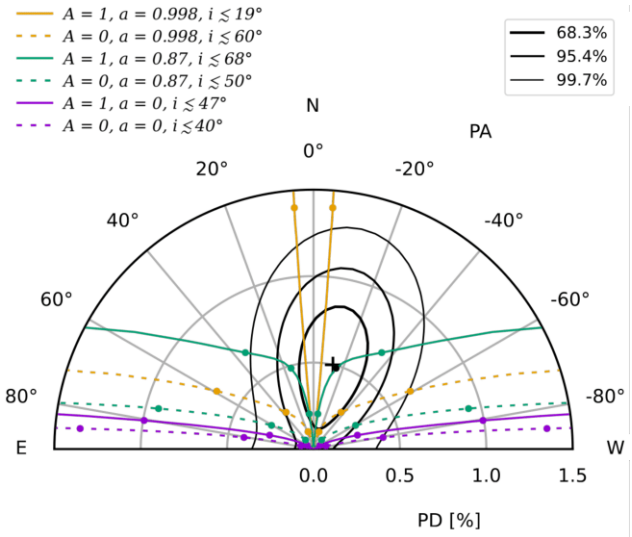

Fig. 21. Modeling PD and PA with a relativistic accretion-disk model KYNBRR for different BH spin values, a = 0 (violet), a = 0.87 (green), and a = 0.998 (orange), considering albedo A = 0 (no reflectivity, dashed lines) and A = 1 (maximal reflectivity of returning radiation, solid lines). Values for inclinations of 20, 40 and 60 deg are denoted by bullets. Corresponding upper limits for inclination are taken from the intersections with the 3 σ contour line. The black bullet shows the case of a = 0.87 and inclination i = 40 deg, corresponding to the best-fit spectral results, and it is very close to the best-fit values of PD and PA from the IXPE data denoted by a black cross.

Svoboda J., Dovčiak M., Steiner J. et al. (2024). Dramatic Drop in the X-Ray Polarization of Swift J1727.8–1613 in the Soft Spectral State. ApJ, 966L, 35S, https://ui.adsabs.harvard.edu/abs/2024ApJ...966L..35S/abstract.

We report on detection of X-ray polarisation in the black-hole X-ray binary Swift J1727.8–1613 during its dim hard spectral state by the Imaging X-ray Polarimetry Explorer (IXPE). This is the first detection of X-ray polarisation at the transition from the soft to the hard state in a black-hole X-ray binary. We found an averaged 2-8 keV polarisation degree of (3.3 ± 0.4)% and a corresponding polarisation angle of 3° ±4°, which matches the polarisation detected during the rising stage of the outburst, in September-October 2023, within 1σ uncertainty. The observational campaign complements previous studies of this source and enables comparison of the X-ray polarisation properties of a single transient across the X-ray hardness-intensity diagram. The complete recovery of the X-ray polarisation properties, including the energy dependence, came after a dramatic drop in the X-ray polarisation during the soft state. The new IXPE observations in the dim hard state at the reverse transition indicate that the accretion properties, including the geometry of the corona, appear to be strikingly similar to the bright hard state during the outburst rise despite the X-ray luminosities differing by two orders of magnitude.

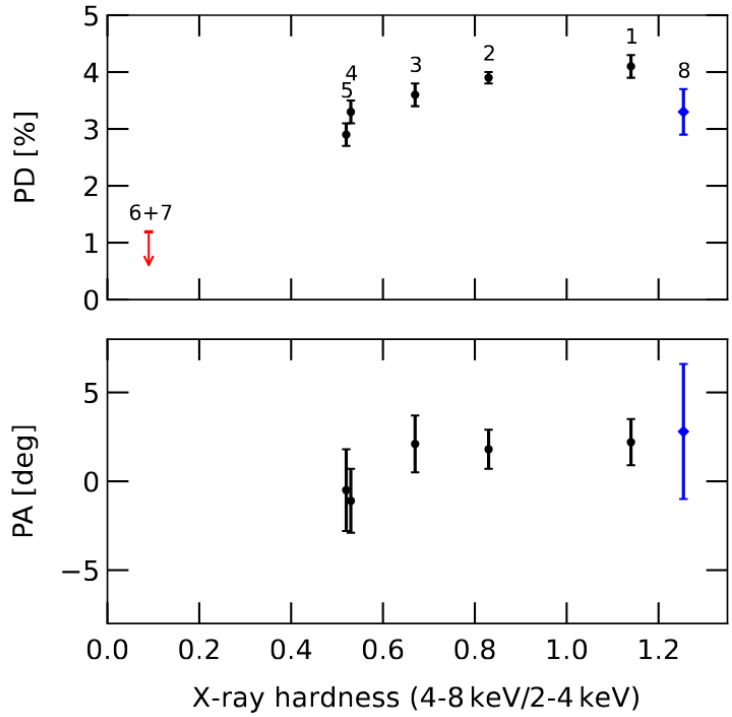

Fig. 22. The evolution of polarisation degree and angle on the spectral X-ray hardness reveals a significant dependence of the polarisation properties on the accretion state. The first observations 1–5 of the peak outburst (Veledina et al. 2023; Ingram et al. 2024) are shown in black. The red arrow signifies the 1.2% upper limit on the PD (with the PA unconstrained) at the 99% confidence level, as obtained in the soft state (observations 6 and 7 combined; Svoboda et al. 2024). Observation 8 of the dim hard state is shown in blue with polarimetric properties similar to the bright hard state.

Faculty of Mathematics and Physics of the Charles University (FMP CU):

Thermodynamic properties downstream of interplanetary shocks

We investigated the thermodynamic properties downstream of interplanetary shocks. Changes in temperature, density, and specific entropy were studied, considering the shock geometry in the expanding solar wind and the limitations imposed by single-point measurements. Our approach resolves previous contradictions in the temperature and specific entropy profiles in downstream regions and demonstrates enhanced turbulent heating relative to the pristine solar wind, potentially contributing significantly to the overall heating of the solar wind plasma.

Pitňa, A.; Šafránková, J.; Němeček, Z.; Pi, G.; Zank, G.; Zhao, L.; Adhikari, L.; Nakanotani, M.: Turbulent Heating of Solar Wind Plasma Downstream of Magnetohydrodynamic Shocks, Astrophys. J., 963(2), 161, doi: 10.3847/1538-4357/ad1c64, 2024.

Modification of the power spectral density of magnetic field fluctuations by quasiperpendicular interplanetary shocks

We investigate the role of interplanetary (IP) shocks in solar wind turbulence using observations of Solar Orbiter, Parker Solar Probe, and Wind. Employing statistical analysis of quasi-perpendicular fast forward (FF) and fast reverse (FR) shocks, we revisit evolution of magnetic field turbulence across IP shocks. Our findings suggest that the observed spectral modification is primarily governed by changes in turbulence Alfvénicity, not directly by dissipation processes related to the shock, and can be commonly observed toward extensive heliospheric distances.

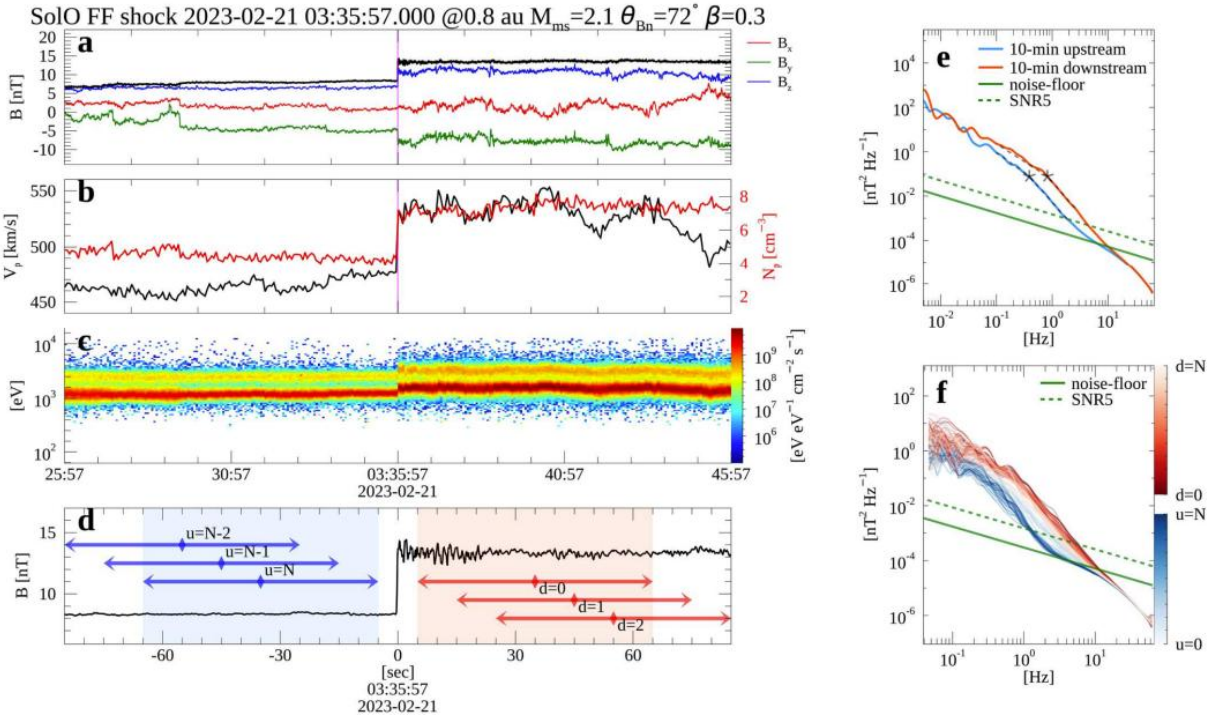

Figure 23. Example of FF IP shock observed by SolO on 2023 February 21. Magnetic field upstream and downstream power spectra on the right panels.

Park, B; Pitňa, A; Šafránková, J; Němeček, Z: Modification of the Power Spectral Density of Magnetic Field Fluctuations by Quasi-Perpendicular Interplanetary Shocks, Astrophys. J. Lett., 986 (2): Art. No. L30, doi:10.3847/2041-8213/ade25b, 2025.

Observation of proton and alpha particle parameter evolution at the fast wind stream interface

We investigated rarefaction regions in the solar wind, which occur on the trailing edges of fast solar wind streams, ahead of the slow solar wind behind them. We employed superposed epoch analysis to reveal the gradual evolution of both proton and alpha-particle parameters. We showed that a corresponding composition boundary can be defined, where the relative abundance of alpha particles and the alpha-proton temperature ratio abruptly change from fast solar wind to slow solar wind values, consistent with the stream interface.

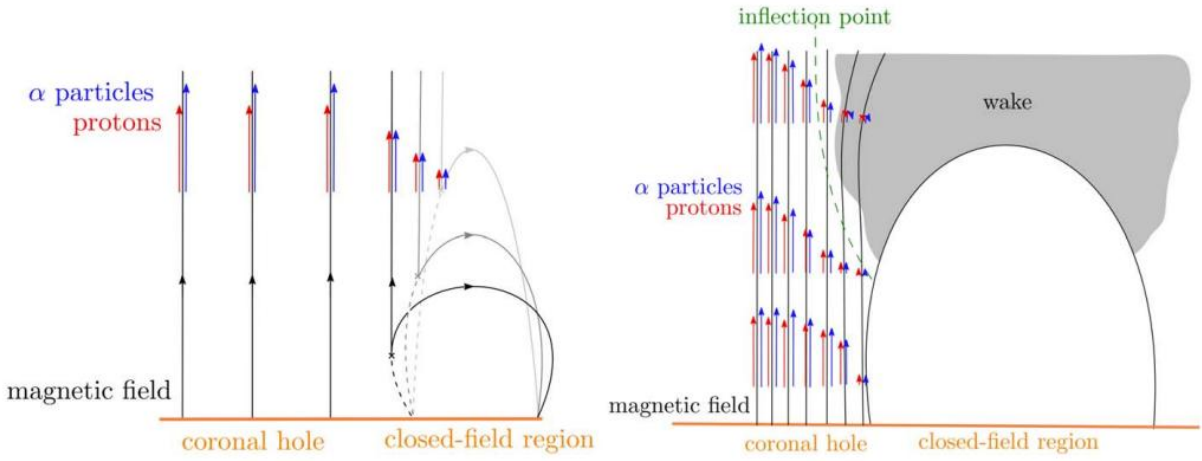

Figure 24. Sketch of two proposed scenarios of the rarefaction region formation during the initial phase of the solar wind expansion.

Ďurovcová, T.; Šafránková, J.; Němeček, Z.: How Does the Structure of Rarefaction Regions Develop? Astrophys. J., 966(1), 81, 10.3847/1538-4357/ad3074, 2024.

Investigations of plasma depletion events at Martian ionosphere

We investigated the spatial scales and temporal extents of plasma depletion events, recently discovered regions in the Martian ionosphere characterized by a more than an order-of-magnitude decrease in plasma density. Using combined measurements from the MAVEN and Mars Express spacecraft, we demonstrate that these events can extend over distances of up to 750 km and persist for several hours. Importantly, they appear to reform at the same location on the following day. Such large-scale, recurring phenomena may potentially play a significant role in ionospheric loss.

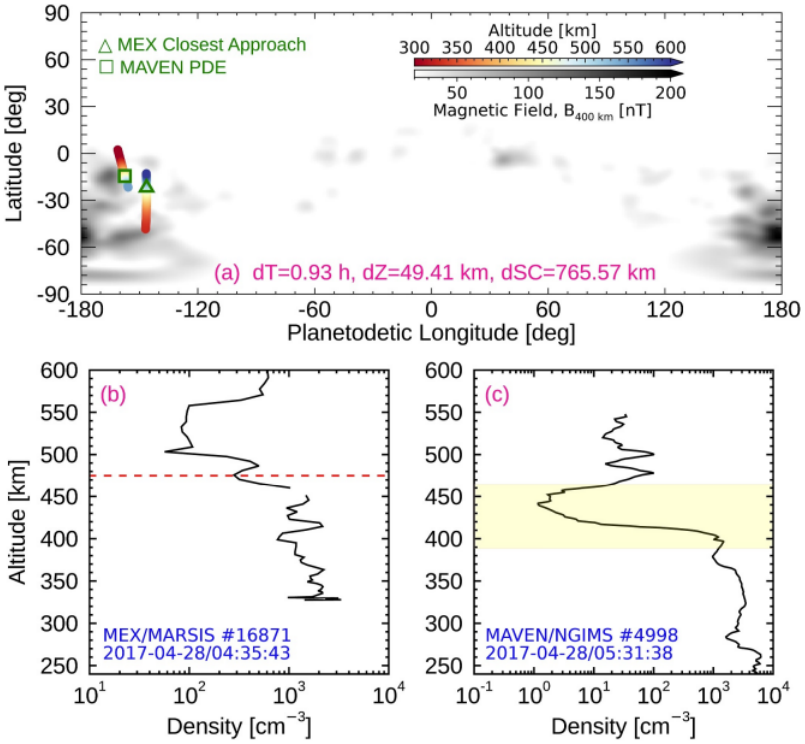

Figure 25. Orbital traces of MEX and MAVEN projected onto planetary longitude-latitude coordinates, with altitude indicated by a color-coded scale. The green colored square indicates the peak depletion altitude of the PDE, while the green colored triangle marks MEX's closest approach to it. Both depletion event observations are separated about 56 min in time, ≈766 km in distance, and an altitude difference of around 49 km.

Basuvaraj, P., Němec, F., Fowler, C. M., Regoli, L. H., Němeček, Z., Šafránková, J., Witasse, O., Wilson, C. F., Spatial and Temporal Extent of Plasma Depletion Events in the Ionosphere of Mars, J. Geophys. Res. Planets, 130(10), 10.1029/2025JE008934, 2025.